A multi-horizon Peridynamics for coupled fluid flow and heat transfer

Changyi Yang[1], Jidong Zhao[1*], Fan Zhu[2], Ruofeng Feng[1]

[1] Department of Civil and Environmental Engineering, The Hong Kong University of Science and Technology, HKSAR, China

[2] Department of Urban Management, Kyoto University, Kyoto, Japan

* Corresponding author, jzhao@ust.hk

Abstract

This paper presents a Peridynamics-based computational approach for modeling coupled fluid flow and heat transfer problems. A new thermo-hydrodynamic Peridynamic (PD) model is formulated with the semi-Lagrangian scheme and non-local operators. To enhance accuracy and numerical stability, a multi-horizon scheme is developed to introduce distinct horizons for the flow field and thermal field. The multi-horizon scheme helps to capture the convective zone and complex thermal flow pattern while effectively mitigating possible oscillations in temperature. We validate the computational approach using benchmarks and numerical examples including heat conduction, natural convection in a closed cavity, and Rayleigh-Bénard convection cell. The results demonstrate that the proposed method can accurately capture typical thermal flow behaviors and complex convective patterns. This work offers a new foundation for future development of a unified PD framework for robust, comprehensive multi-physics analysis of thermal fluid-solid interaction problems with complex evolving discontinuities in solids.

Keywords: Multi-physics, Peridynamics, fluid flow, convection, computational modeling.

1 Introduction

Coupled fluid flow with heat transfer is a complex and intriguing physical process found in various natural and engineered systems. It involves simultaneous interactions between fluid motion and thermal energy transfer. This coupling plays a crucial role in many practical applications, from engineering processes to natural phenomena like ocean currents and atmospheric circulation. For example, in designing heat exchangers and solar collectors (Du et al., 2024), accurate predictions of fluid flow and heat transfer rates are vital for efficient heat exchange between different fluid streams and solid structures. Similarly, in aerospace engineering, understanding the interaction between fluid flow and heat transfer is crucial for assessing the thermal loads on aircraft surfaces during flight (van Heerden et al., 2022). Studying coupled fluid flow and heat transfer presents challenges due to the complicated phenomena involved, including convective heat transfer, boundary layer development, fluid mixing, and thermal stratification. The convection processes to be discussed in this paper can be categorized into two types based on the driving forces behind fluid motion. Natural convection arises from buoyancy force caused by temperature variations, while forced convection results from pressure or viscous force applied on the fluid boundary. Most convective problems in practice involve a combination of both types.

Various mesh-based numerical methods have been developed to better understand the complex interplay between fluid dynamics, thermal energy transport, and boundary conditions for realistic modeling of coupled process. Gartling (1977) employed the Galerkin finite element method (FEM) to solve the Navier-Stokes equation coupled with the energy equation, assuming the fluid was assumed to be incompressible and applying the Boussinesq approximation. The work examined thermal flow near a heat exchanger and in a cylindrical enclosure. Similar problems have been investigated using least-square FEM (Bell & Surana, 1995; Prabhakar & Reddy, 2006; Tang & Tsang, 1997; Wang & Qin, 2018). To accommodate the three-dimensional (3D) complexity inherent in fluid dynamics, Mallinson & Davis (1977) derived the solution of 3D Navier-Stokes equation within a box by finite difference method (FDM). The solution explored the 3D fluid motion generated by side heating from the box's surface. Later, by using a second-order central difference scheme and special extrapolation with variable discretization, De Vahl Davis (1983) provided a benchmark solution for 2D natural convection problem, in which accurate predictions were achieved for fluid flow with Rayleigh number up to 10^6. FDM was also employed in more specific scenarios such as natural convection in shallow cavity (Cormack et al., 1974; Drummond & Korpela, 1987) and turbulent convection (Paolucci, 1990; Trias et al., 2007). The effects of an enclosed circle on thermal flow in a rectangular cavity were studied by Angeli et al. (2008) and Kim et al. (2008) using the finite volume method (FVM) and immersed boundary method, which

effectively capture the thermal flow field between the cooler outer rectangular enclosure and the hotter inner circular boundary.

Recently, thermal flow coupling has been addressed using various particle-based methods. These methods do not rely on a fixed mesh structure, which reduces the computational costs associated with re-meshing and are hence well-suited for modeling complex geometries and free surface flow. Among these methods, smoothed particle hydrodynamics (SPH) has gained popularity for coupled thermal flow modeling. Cleary & Monaghan (1999) were the first to successfully implement thermal fields in SPH, although their work focused solely on heat conduction. Szewc et al. (2011) and Danis et al. (2013) explored natural convection in a square enclosure using SPH and examined the effects of Rayleigh number, Prandtl number, and Gay-Lussac number. Their findings indicated that fluid flow transits gradually from laminar flow to turbulent flow as Rayleigh number increases up to 10^6. More recently, SPH has been effectively applied to model natural convection in complex geometries, such as a square closure with an inner circular hole (Aragón et al., 2021), concentric annuli (Garoosi & Shakibaeinia, 2020; Yang & Kong, 2019; Zhang & Yang, 2022) and reactor core with internal channels (Gui et al., 2022). More recently, Reece et al. (2024) extended the coupled SPH method to multi-phase condition by considering thermal stratification of different components. In addition to SPH, other particle-based methods have emerged. For instance, Gao & Oterkus (2019) leveraged the non-local operators proposed by Madenci et al. (2019) to simulate natural and mixed convection non-locally, achieving good agreements in temperature and velocity with SPH results.

Peridynamics (PD), introduced by Silling (2000) and further developed by Silling et al. (2007), is a relatively new Lagrangian method based on the concept of particle interactions. It is a widely recognized that PD offers advantages over other meshfree or mesh-based methods, particularly in its ability to model complex evolving discontinuities. By employing integral form governing equations instead of differentials, PD is inherently well-suited for modeling fracturing processes in brittle materials. These include phenomena such as grain crushing (Shi et al., 2022; Zhu & Zhao, 2019a, 2019b), thermally-induced fracturing (Bazazzadeh et al., 2020; Bie et al., 2024a; Bie et al., 2024b; Chen et al., 2021; Gao & Oterkus, 2019a; Hao et al., 2024; Wang et al., 2018; Yang et al., 2024a; Zhang & Zhang, 2022), and impact-induced fracturing (Yao et al., 2023; Yao & Huang, 2022; Zhu & Zhao, 2021). While PD has shown significant capability in addressing discontinuities in solid mechanics, literature on its application to fluid flow is limited. Recently, a new version of PD, named Eulerian PD (Silling et al., 2017) or semi-Lagrangian PD (Behzadinasab & Foster, 2020), has emerged. This approach uses the deformed body as the reference configuration rather than undeformed one, showing promise for modeling fluid flow and large deformation problems. The authors have recently extended the PD framework to include fluid flow and fluid-solid

interaction modeling by coupling total- and semi-Lagrangian formulations of PD (Yang et al., 2024b). However, to the best of the authors' knowledge, there is currently no PD approach available for modeling coupled flow and heat transfer processes, especially when thermal fluid-solid interaction problems are involved with evolving discontinuities in solids.

This study presents a cutting-edge effort to establish a unified PD framework that integrates both fluid dynamics and energy exchanges. A novel coupled thermo-hydrodynamic PD model will be developed using a semi-Lagrangian formulation within the state-based PD framework. The formulation accommodates non-isothermal conditions by incorporating a non-local form energy equation. A multi-horizon scheme is introduced for improving numerical accuracy and stability. The work presented here lays the groundwork for future development of a fully coupled thermo-hydro-mechanical (THM) PD framework, which will provide unique capabilities for modeling coupled THM processes involving large deformation, fracturing in solids, and fluid flow in fractured media. Typical examples include frost cracking and slope failure induced by freezing and thawing (Chen et al., 2024a; Chen et al., 2024b; Yu et al., 2024a, 2024b, 2024c), cool water injection into hot rock formations for oil extraction (Xue et al., 2023), and magma-driven fracturing (Spence & Turcotte, 1985; Taddeucci et al., 2021).

The structure of this paper is organized as follows: Section 2 introduces the fundamental concepts of PD theory, discussing both total- and semi-Lagrangian formulations. Building upon this foundation, Section 3 presents our proposed novel thermo-hydrodynamic PD model. Section 4 details the integration scheme for the PD model to facilitate implementation and computation. Sections 5 and 6 provide a comprehensive set of benchmark and numerical examples, including investigations into heat conduction, natural convection, and Rayleigh-Bernard convection cell. Finally, Section 7 concludes the paper by summarizing the key findings and implications of our study, along with a discussion of potential limitations and outlook.

2 Peridynamics theory and non-local operators

The PD approach is based on the fundamental principle of modeling interactions among individual material points. In this framework, a continuous medium is represented by discretizing it into a finite number of material points. During this discretization process, a specific range known as the *horizon* is defined, which sets the extent of the interaction forces between a master material point and its neighboring points. The set of all neighboring points associated with a given master material point, denoted as Ω_x, is referred to as its *family*. Consequently, the equation of motion for each material point $\boldsymbol{x}$ can be expressed by considering all interactions within its family, as follows:

$$\rho(\boldsymbol{x})\ddot{\boldsymbol{u}}(\boldsymbol{x},t)=\int_{\Omega_x}[\boldsymbol{T}\langle\boldsymbol{x}'-\boldsymbol{x}\rangle-\boldsymbol{T}\langle\boldsymbol{x}-\boldsymbol{x}'\rangle]\,\mathrm{d}V_{x'}+\boldsymbol{b}(\boldsymbol{x}) \tag{1}$$

where ρ, $\boldsymbol{u}$ and $\boldsymbol{b}$ represent the density, displacement and body force density of a master material point, respectively, and $V_{x'}$ represents the volume of a neighboring point. $\boldsymbol{T}$ is defined as the force state, which operates on each bond and yields the interaction forces between different material points. For example, $\boldsymbol{T}\langle\boldsymbol{x}'-\boldsymbol{x}\rangle$ denotes the force exerting from point $\boldsymbol{x}'$ on point $\boldsymbol{x}$.

Force state $\boldsymbol{T}\langle\boldsymbol{x}'-\boldsymbol{x}\rangle$ can be quantified in different ways through constitutive models. For brittle-elastic materials, a typical model is the linear PD solid model given as (Silling et al., 2007)

$$\boldsymbol{T}\langle\boldsymbol{x}'-\boldsymbol{x}\rangle=t\frac{\boldsymbol{Y}}{\|\boldsymbol{Y}\|} \tag{2}$$

in which t is a scalar force state; $\boldsymbol{Y}$ is the deformed bond vector between two material points. Note that for the linear PD solid model given in Eq. (2), the magnitude of $\boldsymbol{T}\langle\boldsymbol{x}'-\boldsymbol{x}\rangle$ may not be the same as $\boldsymbol{T}\langle\boldsymbol{x}-\boldsymbol{x}'\rangle$ and this formulation is commonly known as the state-based PD. If the magnitude of interaction forces between two material points are always equal, the state-based PD reduces to bond-based PD. State-based PD is adopted throughout this paper as it frees many limitations of the bond-based PD (Silling et al., 2007).

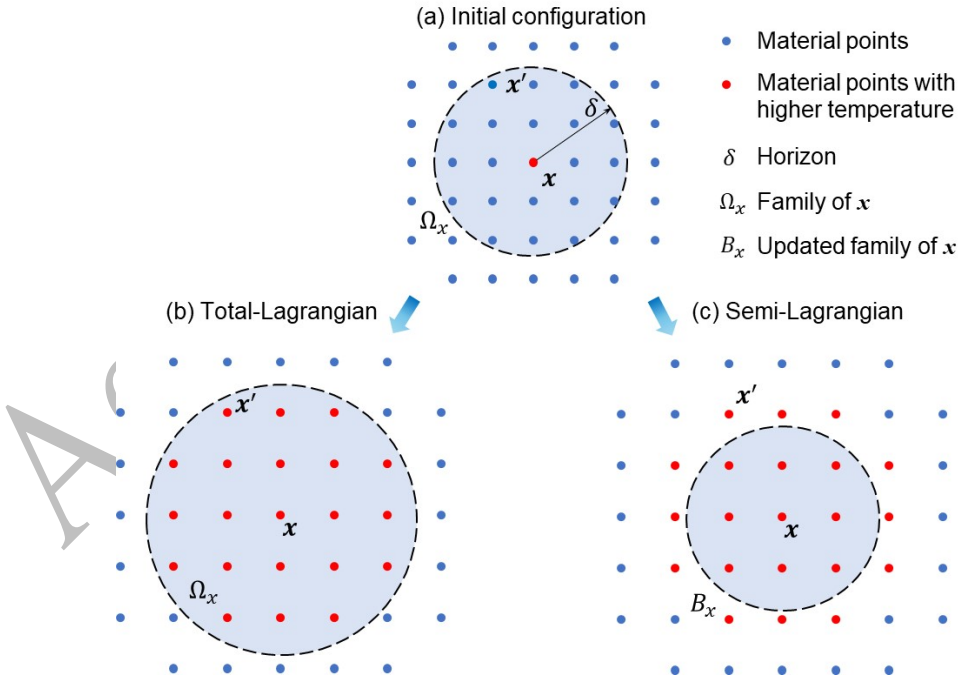

Fig. 1. Schematics of: a) basic concepts and initial configuration of PD; b) total-Lagrangian scheme; and c) semi-Lagrangian scheme by taking thermal expansion process as an example.

As an alternative formulation to the classical solid mechanics, the original PD employed the Lagrangian scheme, as illustrated in Fig. 1(b). In this scheme, neighboring material points for a specific master point stay fixed, while the shape and size of the family evolve continually with deformation. The Lagrangian formulation is well-suited for solid mechanics applications where small deformation assumption usually remains valid. However, it faces challenges when applied to fluid mechanics and problems involving significant deformation, as the shape of the family can become highly distorted. Under such circumstance, the derivatives in the governing equations are poorly evaluated by integration over material points within a distorted family. Semi-Lagrangian PD serves as a remedy to facilitate modeling of large deformation problems by PD. Also known as Eulerian PD (Silling et al., 2017) or updated Lagrangian PD (Bergel & Li, 2016; Tu & Li, 2017; Yan et al., 2019, 2021), it represents a relatively new variant of the traditional PD approach that combines both Lagrangian material points and Eulerian grids. In the semi-Lagrangian PD formulation, material points are still tracked using a Lagrangian approach, meaning their positions, velocities, and accelerations are explicitly updated at each time step. However, the interactions among the material points are computed using a Eulerian framework, where a fixed family shape is maintained, as illustrated in Fig. 1(c). This approach requires updating neighboring material points in the presence of significant deformation, and derivatives are approximated using non-local integral operators. Two commonly used non-local operators are the non-local gradient operator $\mathbb{G}$ and the non-local divergence operator $\mathbb{D}$, which can be expressed as follows (Bergel & Li, 2016)

$$\mathbb{G}(\boldsymbol{A}) = \left[\int_{B_x} w\langle\|\boldsymbol{Y}\|\rangle(\Delta\cdot\boldsymbol{A})\otimes\boldsymbol{Y}\,\mathrm{d}V_{x'}\right]\boldsymbol{M}_x^{-1} \cong \nabla\boldsymbol{A} \tag{3}$$

$$\mathbb{D}(\boldsymbol{A}) = \int_{B_x} w\langle\|\boldsymbol{Y}\|\rangle(\Delta\cdot\boldsymbol{A})\cdot(\boldsymbol{M}_x^{-1}\boldsymbol{Y})\,\mathrm{d}V_{x'} \cong \nabla\cdot\boldsymbol{A} \tag{4}$$

where $\boldsymbol{A}$ is a random vector; $\Delta\cdot$ represents a difference operator, for example $\Delta\cdot\boldsymbol{A} = \boldsymbol{A}_{x'} - \boldsymbol{A}_x$; $\nabla\boldsymbol{A}$ and $\nabla\cdot\boldsymbol{A}$ represents the local gradient and local divergence of vector $\boldsymbol{A}$, respectively; $\otimes$ is the dyadic product; $\boldsymbol{M}_x$ is defined as the shape matrix, which is calculated as

$$\boldsymbol{M}_x = \int_{B_x} w\langle\|\boldsymbol{Y}\|\rangle\,\boldsymbol{Y}\otimes\boldsymbol{Y}\,\mathrm{d}V_{x'} \tag{5}$$

in which $w\langle\|\boldsymbol{Y}\|\rangle$ is the weight function that determines the influence of neighboring material points based on their distances to the master point. The weight function can be chosen in various

forms, such as unity, B-spline, or Gaussian functions. In this study, $w\langle\|\boldsymbol{Y}\|\rangle$ is specifically selected in the Gaussian from

$$w\langle\|\boldsymbol{Y}\|\rangle = e^{-\left(\frac{\|\boldsymbol{Y}\|}{\alpha\delta}\right)^2} \tag{6}$$

where the parameter α is selected to be 0.5. Note that all the integrations in Eqs. (3)-(5) are conducted over the updated family B_x.

3 Coupled thermo-hydrodynamic Peridynamics model

In this section, the governing equations for fluid flow coupled with heat transfer are reformulated into their non-local forms using the semi-Lagrangian PD method and non-local operators. The fluid flow is assumed to be weakly compressible, inviscid, and heat conducting.

3.1 Continuity equation

The continuity equation required the conservation of mass within a fixed volume over time, which is given by

$$\frac{\partial\rho}{\partial t} + \nabla\cdot(\rho\boldsymbol{v}) = 0 \tag{7}$$

where $\boldsymbol{v}$ is the velocity vector; $\partial/\partial t$ is the Eulerian derivative with respect to time. The term $\nabla\cdot(\rho\boldsymbol{v})$ can be further expanded into

$$\frac{\partial\rho}{\partial t} + \boldsymbol{v}\cdot\nabla\rho + \rho\nabla\cdot\boldsymbol{v} = 0 \tag{8}$$

for isothermal flows, the density change, i.e., the second term on the left-hand side of Eq. (8), can be neglected. However, for thermal flows, where temperature variations occur, the density becomes a thermodynamic variable that is dependent on temperature. Therefore, all three terms in Eq. (8) should be explicitly considered for thermal flow.

To bridge the Eulerian and Lagrangian descriptions (note that semi-Lagrangian PD still adopts Lagrangian description), Lagrangian derivative (also known as material derivative) is introduced as

$$\frac{\mathrm{D}}{\mathrm{D}t} = \frac{\partial}{\partial t} + \boldsymbol{v}\cdot\nabla \tag{9}$$

and therefore, the continuity equation given in Eq. (8) can be alternatively written in Lagrangian form as

$$\frac{\mathrm{D}\rho}{\mathrm{D}t} + \rho\nabla\cdot\boldsymbol{v} = 0. \tag{10}$$

Note that Eq. (10) and Eq. (8) are fundamentally equivalent. The Lagrangian derivative (or material derivative) explicitly incorporates both the local change present in the Eulerian derivative and the convective change terms. This equivalence arises because the material derivative accounts for the temporal variation at a fixed point (local change) and the transport of the quantity due to fluid motion (convective change). Thus, the two formulations describe the same physical process but from different perspectives.

In the case of incompressible flows, directly implementing Eq. (10) in an explicit scheme necessitates an extremely small time step, which is computationally prohibitive. To address this issue, a weakly compressible method proposed by Monaghan (1994) in SPH is utilized to model the incompressible fluid. In this approach, an equation of state is introduced to describe the relationship between the pressure p and the density ρ of the fluid as

$$p = \frac{\rho c_0^2}{n}\left[\left(\frac{\rho}{\rho_0}\right)^n - 1\right] \tag{11}$$

where n is one fitting parameter, which can be interpreted from experiments; ρ_0 is the initial density; c_0 is the artificial sound speed. By using the weakly compressible method, the density is updated according to Eq. (10) and the pressure is calculated explicitly from Eq. (11). Substituting the non-local divergence operator given in Eq. (4) into Eq. (10) gives the non-local continuity equation as follows

$$\frac{\mathrm{D}\rho}{\mathrm{D}t} = -\rho\int_{B_x}\omega\langle\|\boldsymbol{Y}\|\rangle\,\boldsymbol{v}\,\langle\boldsymbol{Y}\rangle\cdot(\boldsymbol{M}_x^{-1}\boldsymbol{Y})\,\mathrm{d}V_{x'} \tag{12}$$

3.2 Momentum equation

The classical local equation of motion is mathematically expressed as

$$\frac{\partial\rho\boldsymbol{v}}{\partial t} + \nabla\cdot(\rho\boldsymbol{v}\otimes\boldsymbol{v}) = \nabla\cdot\boldsymbol{\sigma} + \boldsymbol{b} \tag{13}$$

where $\boldsymbol{\sigma}$ is the Cauchy stress tensor; $\boldsymbol{b}$ denotes the body force density. Eq. (13) governs the motion of a continuous media and is more commonly known as *Navier* equation in fluid mechanics. For

incompressible fluid, Eq. (13) can be further simplified by expanding the two derivatives on the left side

$$\rho\left(\frac{\partial \boldsymbol{v}}{\partial t}+\boldsymbol{v}\nabla\cdot\boldsymbol{v}\right)=\nabla\cdot\boldsymbol{\sigma}+\rho\boldsymbol{g} \tag{14}$$

or expressed in the Lagrangian description with material derivative

$$\rho\frac{\mathrm{D}\boldsymbol{v}}{\mathrm{D}t}=\nabla\cdot\boldsymbol{\sigma}+\rho\boldsymbol{g} \tag{15}$$

In the case of thermal flow, temperature variations can lead to changes in fluid properties such as density and viscosity. The Boussinesq approximation is a commonly adopted approach in which the variations of all fluid properties, except for density differences multiplied by the acceleration due to gravity, i.e., $\rho\boldsymbol{g}$ in Eqs. (14)-(15), are neglected. This approximation allows for a computationally efficient simulation while effectively capturing the buoyancy force resulting from temperature changes. However, it is important to note that the Boussinesq approximation requires small variations in both temperature and density to be valid. In this study, instead of using the Boussinesq approximation, we update the density in each step according to Eq. (10) and then consider the thermal effect by incorporating the following expression

$$\rho=\rho'+\Delta\rho \tag{16}$$

where ρ' denotes the initial density obtained directly from Eq. (10) at each step and $\Delta\rho$ is the variation of density induced by variation in temperature. Provided that the variation in density is linearly related to the variation in temperature, $\Delta\rho$ can be expressed as a function of thermal expansion coefficient β as

$$\Delta\rho=-\beta\Delta\Theta\rho' \tag{17}$$

in which $\Delta\Theta$ is the variation in temperature. Note that the density is assumed to decrease monotonically as temperature increases. If the density-temperature relationship is nonlinear and requires a more complex expression, it is possible to introduce more intricate equations to capture the behavior accurately (Szewc et al., 2011).

The momentum equation can also be expressed in non-local form by substituting Eq. (4) into Eq. (15)

$$\rho\frac{\mathrm{D}\boldsymbol{v}}{\mathrm{D}t}=\int_{B_x}\omega\langle\|\boldsymbol{Y}\|\rangle\left(\boldsymbol{\sigma}_x\boldsymbol{M}_x^{-1}+\boldsymbol{\sigma}_{x'}\boldsymbol{M}_{x'}^{-1}\right)\boldsymbol{Y}\,\mathrm{d}V_{x'}+\boldsymbol{b} \tag{18}$$

3.3 Constitutive equation of fluid

For Newtonian fluid considered in this paper, the stress tensor $\boldsymbol{\sigma}$ in Eq. (15) can be decomposed into two parts

$$\boldsymbol{\sigma} = -p\boldsymbol{I} + 2\mu\dot{\boldsymbol{\varepsilon}} \tag{19}$$

where the pressure p represents the hydrostatic part and can be calculated by the equation of state defined in Eq. (11); μ is dynamic viscosity and $\dot{\boldsymbol{\varepsilon}}$ is the rate of deformation, the product of which denotes the viscous part. $\dot{\boldsymbol{\varepsilon}}$ can be related to the gradient of velocity as

$$\dot{\boldsymbol{\varepsilon}} = \frac{1}{2}[\nabla\boldsymbol{v} + (\nabla\boldsymbol{v})^{\mathrm{T}}] \tag{20}$$

3.4 Energy equation

When considering heat transfer, the fluid flow system is extended by incorporating the energy equation, which states that the time rate of change of the total energy

$$\rho\left(\frac{\partial e}{\partial t} + \boldsymbol{v}\nabla\cdot e\right) = -\nabla\cdot\boldsymbol{q} + \varphi + \rho\Theta_{\mathrm{b}} \tag{21}$$

where Θ_{b} is the internal volumetric heat generation per unit mass; dissipation function $\varphi = 2\mu\dot{\boldsymbol{\varepsilon}}:\dot{\boldsymbol{\varepsilon}}$ is adopted according to Reddy & Gartling (2010); the heat flux $\boldsymbol{q}$ is defined as

$$\boldsymbol{q} = -k_{\mathrm{h}}\nabla\Theta \tag{22}$$

in which k_{h} is the thermal conductivity. For the internal energy function e, one of the most common expressions is as a function of temperature and density, i.e., $e = e(\Theta, \rho)$. The derivative of e to time can be expanded according to the chain rule as

$$\frac{\partial e}{\partial t} = \frac{\partial e}{\partial \Theta}\frac{\mathrm{D}\Theta}{\mathrm{D}t} + \frac{\partial e}{\partial \rho}\frac{\mathrm{D}\rho}{\mathrm{D}t} \tag{23}$$

where $\partial e/\partial\Theta$ is defined as the specific heat capacity c; and $\mathrm{D}\rho$ can be regarded as zero for incompressible fluid considered in this paper. Therefore, substituting Eq. (23) into Eqs. (21)-(22) yields the non-local energy equation and non-local Fourier's law

$$\rho c\frac{\mathrm{D}\Theta}{\mathrm{D}t} = \int_{B_x}\omega\langle\|\boldsymbol{Y}\|\rangle\left(\boldsymbol{q}_x\boldsymbol{M}_x^{-1} + \boldsymbol{q}_{x'}\boldsymbol{M}_{x'}^{-1}\right)\boldsymbol{Y}\,\mathrm{d}V_{x'} + \varphi + \rho\Theta_{\mathrm{b}} \tag{24}$$

$$\boldsymbol{q_x} = -k_{\mathrm{h}} \left[\int_{B_x} \omega \langle \|\boldsymbol{Y}\| \rangle \, (\Delta \cdot \Theta) \, \boldsymbol{Y} \, \mathrm{d}V_{x'} \right] \boldsymbol{M}_x^{-1} \tag{25}$$

4 Multi-horizon scheme and numerical implementation

Section 3 provides a detailed formulation of the coupled thermo-hydrodynamic PD model, which can be readily used to model convection problems. However, our previous research on the dispersion relation and error analysis of the PD heat equation (Yang et al., 2024a) has highlighted the significant impact of non-locality on the accuracy of thermal field modeling. Specifically, as the horizon size increases, the ratio of heat conduction slows down, and there is a potential for oscillations in the temperature field. This phenomenon occurs because the non-local PD formulation allows particles to bypass heat flux, which is inconsistent with the fundamental nature of heat conduction, a process that is inherently local and relies on direct contact. It is worth noting that the previous investigation was based on a total-Lagrangian scheme, and the situation may be even more challenging with a semi-Lagrangian scheme due to the additional errors arising from irregularly distributed material points. With these considerations, it is favourable to use a small horizon for the thermal field since a small horizon helps mitigate the potential issues associated with non-local effects as mentioned above.

On the other hand, the convection process in thermal flow can exhibit highly non-local behaviour. In fluid flow systems, convection can induce changes in density and velocity profiles throughout the fluid domain. While these changes originate from local heat conduction, they can occur over a larger spatial extent, especially in extreme cases such as Earth's atmosphere and mantle, spanning hundreds of kilometers (Huang, 2024). Since density and velocity are crucial factors in determining flow behaviours of fluids, it is essential to select a horizon size for fluid flow modeling that is large enough to capture the convective characteristics. According to the numerical experiments conducted by Reece et al. (2024), a kernel smoothing length of four times the particle size is required to accurately capture the steady-state thermal flow in SPH. Similarly, based on our experience, it is recommended that the horizon for fluid flow modeling in PD should be at least three times the material point size, with four or five times acceptable, to effectively capture the complex convective pattern. However, this poses a dilemma when it comes to modeling thermal flow, as a smaller horizon is preferable to heat conduction process.

To address the challenge of maintaining accuracy and stability for both fluid and thermal field modeling, a multi-horizon scheme has been employed in this study. This approach, first proposed by Yang et al. (2024a) in coupled thermo-mechanical problems, involves using a larger horizon

for solid fracturing modeling and a smaller horizon for heat transfer modeling. In the context of coupled flow and heat transfer processes, a larger horizon is adopted for modeling fluid motion while a smaller one, termed as *thermal horizon*, is used for heat conduction. The larger fluid horizon captures convective behavior and changes in density and velocity profiles over a larger spatial extent, while the smaller thermal horizon focuses on localized heat conduction and mitigates dispersive issues in thermal modeling. This approach allows us to achieve optimized accuracy in both fluid and thermal aspects by considering their distinct characteristics. The multi-horizon scheme also serves as a way to save computational cost as fewer neighboring material points are involved in the thermal field model. A schematic diagram illustrating the methodology is presented in Fig. 2.

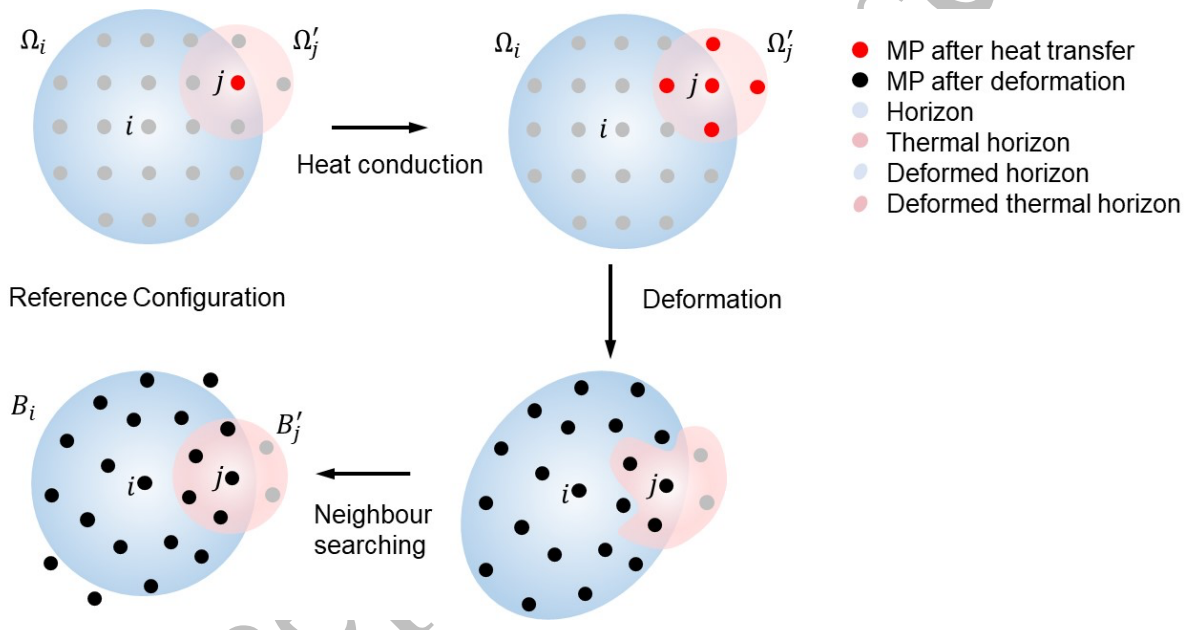

Fig. 2. Schematics of semi-Lagrangian multi-horizon thermo-hydrodynamic PD model: family of material point i (initial Ω_i and updated B_i) and thermal horizon of material point j (initial Ω_j' and updated B_j').

4.1 Spatial discretization

To solve the integral governing equations, the entire simulation domain must be discretized into subdomains. Typically, line segments, squares, and cubes are used as subdomains for 1D, 2D, and 3D problems, respectively. After discretization, material points are placed at the centroids of these subdomains. All calculations are performed at these material points, which are analogous to Gaussian points in the FEM. However, these material points carry all material properties as well as the volume (or area/length for 2D/1D problems) of their respective subdomains. For clarity, Fig.

3 illustrates the discretization of a 2D problem with a uniform spacing Δx between material points. Using this meshless discretization scheme, Eq. (12), Eq. (18), Eq. (24) and Eq. (25) can be expressed in the discretized form as

$$\frac{\mathrm{D}\rho_i}{\mathrm{D}t} = -\rho_i \sum_{j=1}^{N_i} \omega\langle\|\boldsymbol{Y}_{ij}\|\rangle \left(\boldsymbol{v}_j - \boldsymbol{v}_i\right)\cdot\left(\boldsymbol{M}_i^{-1}\boldsymbol{Y}_{ij}\right) V_j\psi_j \tag{26}$$

$$\rho_i \frac{\mathrm{D}\boldsymbol{v}_i}{\mathrm{D}t} = \sum_{j=1}^{N_i} \omega\langle\|\boldsymbol{Y}_{ij}\|\rangle\left(\boldsymbol{\sigma}_i\boldsymbol{M}_i^{-1} + \boldsymbol{\sigma}_j\boldsymbol{M}_j^{-1}\right)\boldsymbol{Y}_{ij}V_j\,\psi_j + \boldsymbol{b}_i \tag{27}$$

$$\rho_i c_i \frac{\mathrm{D}\Theta_i}{\mathrm{D}t} = \sum_{j=1}^{N_i'} \omega\langle\|\boldsymbol{Y}_{ij}\|\rangle\left(\boldsymbol{q}_i\boldsymbol{M}_i^{-1} + \boldsymbol{q}_j\boldsymbol{M}_j^{-1}\right)\boldsymbol{Y}_{ij}V_j\psi_j + \varphi_i + \rho\Theta_{\mathrm{b}i} \tag{28}$$

$$\boldsymbol{q}_i = -k_{\mathrm{h}}\left[\sum_{j=1}^{N_i'} \omega\langle\|\boldsymbol{Y}_{ij}\|\rangle\left(\Theta_j - \Theta_i\right)\boldsymbol{Y}_{ij}V_j\psi_j\right]\boldsymbol{M}_i^{-1} \tag{29}$$

where the subscripts i and j are associated with master material point i and neighboring material point j, respectively. N represents family number within the fluid horizon while N' represents family number within the thermal horizon. The deformed bond vector between i and j, $\boldsymbol{Y}_{ij}$, is calculated by $\boldsymbol{x}_j - \boldsymbol{x}_i$. ψ_j is a volume correction coefficient since the outer neighboring material points within the range of $\delta - \Delta x/2 < \|\boldsymbol{Y}_{ij}\| < \delta$ are only partially enclosed within the horizon as illustrated in Fig. 3. The correction coefficient ψ_j is defined according to the distance between two material points as (Silling & Askari, 2005)

$$\psi_j = \begin{cases} \dfrac{\delta - \Delta x/2 - \|\boldsymbol{Y}_{ij}\|}{\Delta x} & ,\delta - \Delta x/2 < \|\boldsymbol{Y}_{ij}\| < \delta \\ 1 & ,\|\boldsymbol{Y}_{ij}\| \le \delta - \Delta x/2 \end{cases} \tag{30}$$

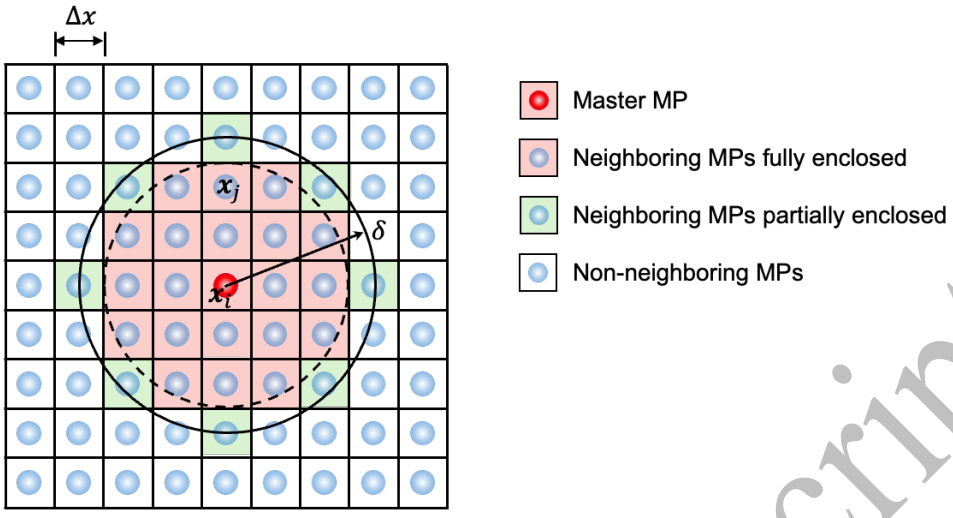

Fig. 3. Discretization, material points and volume correction in a 2D problem.

4.2 Time integration

To numerically obtain the solution to the coupled thermo-hydrodynamic system, the coupled PD equations are partitioned naturally according to fluid flow field and thermal field, and each field is solved sequentially by a forward difference scheme. The procedure involves a series of steps as illustrated in the flow chart in Fig. 4. In each time step, the heat equation is initially solved within the thermal horizon using a forward difference scheme.

$$\rho_i^n c_i \frac{\Theta_i^{n+1} - \Theta_i^n}{\Delta t} = \sum_{j=1}^{N_i'} \omega\langle \|\boldsymbol{Y}_{ij}^n\| \rangle \left(\boldsymbol{q}_i^n \boldsymbol{M}_i^{-1} + \boldsymbol{q}_j^n \boldsymbol{M}_j^{-1}\right) \boldsymbol{Y}_{ij}^n V_j^n \psi_j^n + \varphi_i^n + \rho_i^n \Theta_{\mathrm{b}i}^n \tag{31}$$

where the superscript n denotes the values at n-th step and Δt is the time step. This computation enables the update of temperatures for material points within the thermal horizon while keeping the positions of all material points unchanged.

Subsequently, the continuity and momentum equations are solved within the fluid horizon also by a forward difference scheme

$$\frac{\rho_i^{n+1} - \rho_i^n}{\Delta t} = -\rho_i^n \sum_{j=1}^{N_i} \omega\langle \|\boldsymbol{Y}_{ij}^n\| \rangle \left(\boldsymbol{v}_j^n - \boldsymbol{v}_i^n\right) \cdot \left(\boldsymbol{M}_i^{-1} \boldsymbol{Y}_{ij}^n\right) V_j^n \psi_j^n. \tag{32}$$

In this step, the new temperatures obtained from the heat equation solution are used. The position, velocity, and acceleration of the material points are then updated accordingly by the velocity Verlet scheme

$$\boldsymbol{v}_i^{n+\frac{1}{2}} = \boldsymbol{v}_i^n + \frac{1}{2}\boldsymbol{a}_i^n \Delta t \tag{33}$$

$$\boldsymbol{x}_i^{n+1} = \boldsymbol{x}_i^n + \boldsymbol{v}_i^{n+\frac{1}{2}} \Delta t \tag{34}$$

$$\boldsymbol{a}_i^{n+1} = \frac{1}{\rho_i^{n+1}} \sum_{j=1}^{N} \omega \langle \| \boldsymbol{Y}_{ij}^{n+1} \| \rangle \left(\boldsymbol{\sigma}_i^n \boldsymbol{M}_i^{-1} + \boldsymbol{\sigma}_i^n \boldsymbol{M}_j^{-1} \right) \boldsymbol{Y}_{ij}^{n+1} V_j^n \psi_j^n + \boldsymbol{b}_i^n \tag{35}$$

$$\boldsymbol{v}_i^{n+1} = \boldsymbol{v}_i^{n+\frac{1}{2}} + \frac{1}{2}\boldsymbol{a}_i^{n+1} \Delta t \tag{36}$$

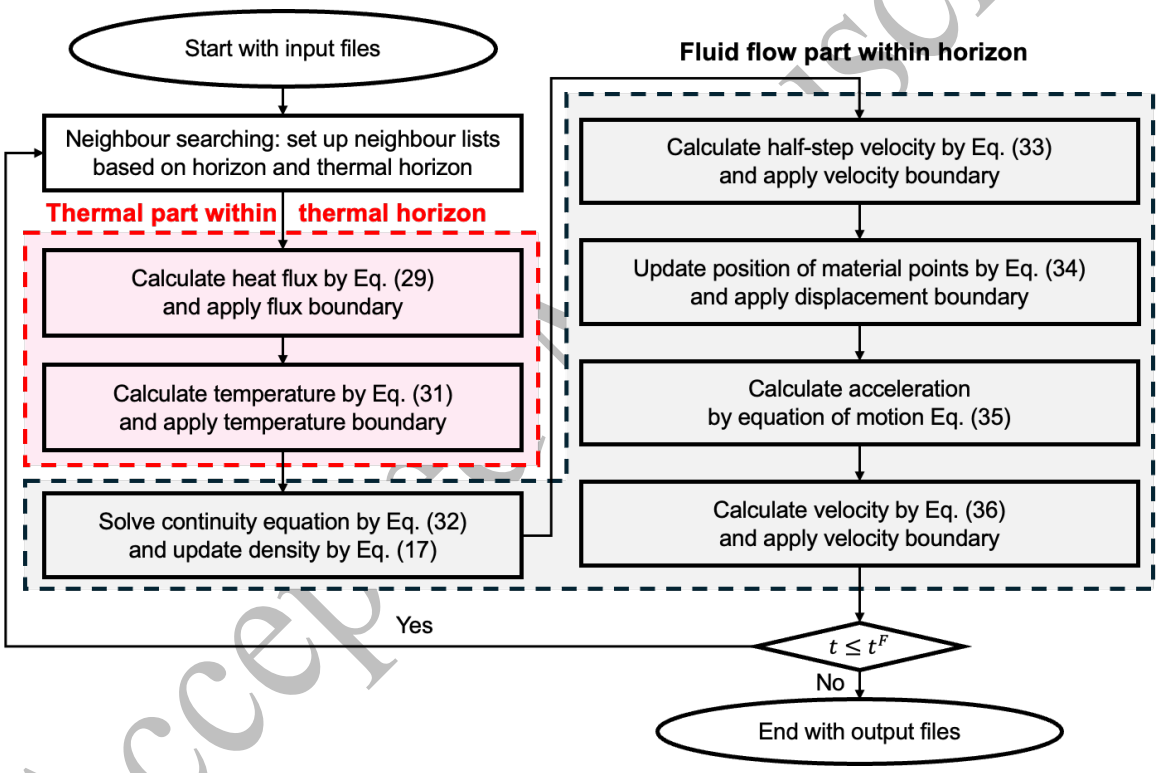

Fig. 4. Flow chart of the time integration of multi-horizon scheme.

In scenarios involving large deformation problems, such as fluid flow, it is important to note that both the fluid horizon and thermal horizon can become significantly distorted after updating the positions of the material points. As a result, an additional neighbor searching process is necessary in the semi-Lagrangian scheme. During this process, the neighboring material points of a given master point are updated while preserving the circular shape of both the fluid horizon and thermal horizon. For a visual representation of the described methodology, readers are referred to

Fig. 2. Since neighbor searching must be performed at each time step due to the continuous motion of material points, selecting an efficient neighbor-searching algorithm is critical for minimizing computational costs. In this study, we adopt the region partition search algorithm, as elaborated in Madenci & Oterkus (2014) and Diyaroglu (2016). The primary concept of the region partitioning algorithm is to divide the entire domain into equally sized cells that are larger than the horizon. When searching for neighbouring material points, it is only necessary to examine the neighbouring cells while deactivating all the material points in non-neighbouring cells. The region partition search algorithm has been proven to outperform several other searching algorithms with different tree structures (Vazic et al., 2020). While there may be more advanced searching algorithms that offer superior computational efficiency, optimizing the searching algorithm is beyond the scope of this paper.

4.3 Implementation of boundary conditions

In numerical simulations, displacement, velocity, and temperature boundary conditions can be directly implemented by introducing additional material points as non-local Dirichlet boundary conditions. For non-isothermal problems, adiabatic or flux boundary conditions are also commonly required. Flux boundary conditions are typically treated as Neumann boundary conditions. Madenci & Oterkus (2014) proposed a method for implementing non-local flux boundary conditions by adding extra material points and prescribing their temperatures at each time step; however, this approach significantly increases computational costs.

In this study, we adopt a two-field formulation of the energy equation, as shown in Eq. (24) and Eq. (25), which explicitly expresses the governing equation for flux. This formulation allows flux boundary conditions to be imposed directly by prescribing the flux (Dirichlet boundary) rather than indirectly through temperature (Neumann boundary). Macek & Silling (2007) recommended that the extent of additional material points should match the horizon size, δ, to ensure that boundary conditions are adequately reflected within the simulation domain. In the multi-horizon scheme used in this work, displacement and velocity boundaries are applied using three layers of material points, while only one layer of material points is sufficient for thermal boundaries.

4.4 Numerical stabilization

Due to the discretized nature of material points in semi-Lagrangian PD, they can sometimes become unevenly distributed or cluster together, leading to inaccurate results or program errors. To mitigate this issue, the particle shifting technique is employed. It involves adjusting the positions of material points during the simulation to alleviate clustering and improve the overall

distribution. The shifting process typically includes two main steps. First, the density of each particle is estimated based on its neighboring material points as

$$\rho = \frac{\int_{B_x} \omega\langle \|\boldsymbol{Y}\| \rangle \, \mathrm{d}m_{x'}}{\int_{B_x} \omega\langle \|\boldsymbol{Y}\| \rangle \, \mathrm{d}V_{x'}} \tag{37}$$

where $m_{x'}$ and $V_{x'}$ represent the mass and volume of a neighbouring material point, respectively. Particles that are too close to each other or have higher densities are shifted or moved slightly to achieve a more uniform distribution. The shifting is performed by applying corrective displacements to each material points as (Yang et al., 2024a)

$$\Delta \boldsymbol{x}_i = C_{\mathrm{PST}} v_{\max} \mathrm{d}t \sum_{j=1}^{N_i} \frac{\left(\frac{1}{N_i}\sum_{j=1}^{N_i} \|\boldsymbol{Y}\|\right)^2}{\|\boldsymbol{Y}\|^2} \boldsymbol{N}\langle \boldsymbol{Y} \rangle \tag{38}$$

where C_{PST} is a shifting coefficient; $v_{\max}$ represents the maximum expected velocity of fluid material points throughout the computational domain; $\boldsymbol{N}\langle \boldsymbol{Y} \rangle$ denotes the unit vector of the deformed bond.

5 Benchmarks

5.1 Pure heat conduction of fluid in a square cavity

The natural convection within a closed square cavity serves as a typical case for modeling convective processes. To validate the proposed multi-horizon thermo-hydrodynamic PD model and semi-Lagrangian scheme for heat transfer, we first simulate pure heat conduction in the same square cavity before attempting to capture convective characteristics.

The schematic illustration of the square cavity is shown in Fig. 5 with both the width and length l equal to 1 m. The initial temperature of the whole cavity is set as 0 °C. The temperatures of the left and right boundaries are fixed at 1 °C and 0 °C, respectively. The upper and lower boundaries are assumed to be adiabatic. All four surfaces are fixed by setting the velocity in both x and y directions to zero. These non-local boundary conditions are applied by adding additional material points outside the modeling domain as shown in Fig. 5(b). Following the multi-horizon scheme, the horizon for fluid flow is adopted to be three times the material point size, while the thermal horizon for heat transfer is chosen as 1.5 times the material point size. Note that for thermal flow modeling, the thermal horizon cannot be adopted as only one time material point size as used in thermo-mechanical problems of solids by Yang et al. (2024a). Owing to the large deformation

nature of fluid flow, the material points can be randomly distributed within the domain. If the thermal horizon is set as only one time point size, there might be no neighboring material points in certain direction and instability problem may be induced. The whole model is consequently discretized into 86×86 Lagrangian material points with each size equal to 0.0125m.

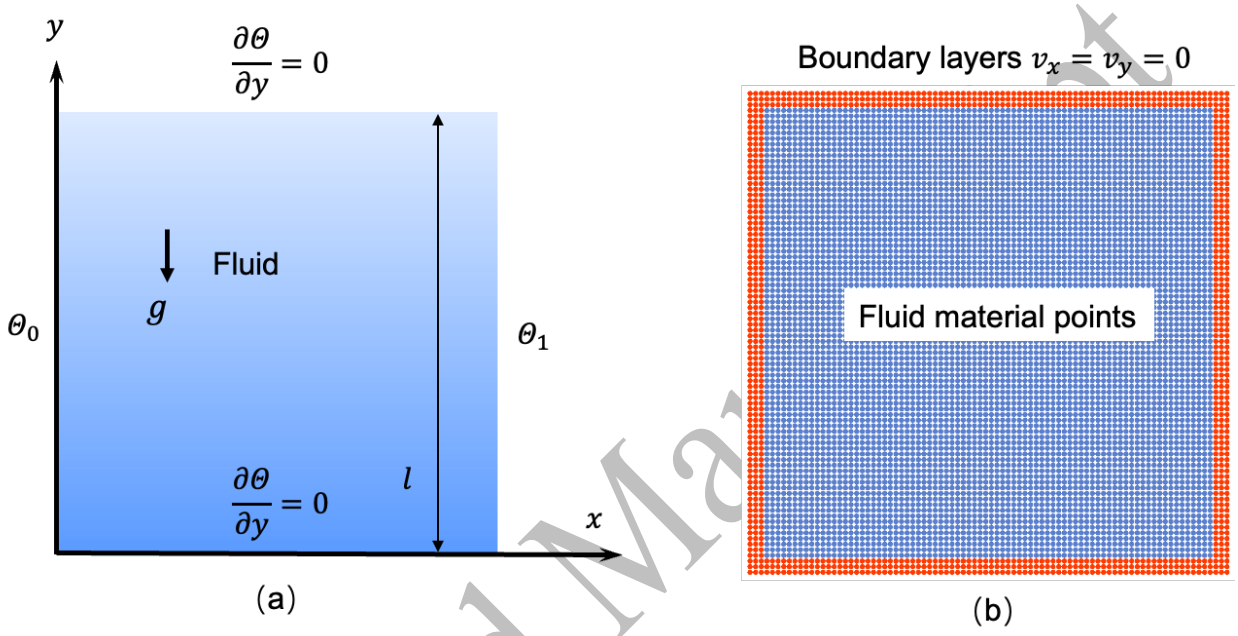

Fig. 5. Natural convection in a closed square cavity: (a) thermal boundary conditions and body force; and (b) discretized PD model and velocity boundary conditions.

The fluid is assumed to be dry air which has the following properties: density $\rho = 1.3082$ kg/m^3, viscosity $\mu = 1.7 \times 10^{-5}$ Pa·s, thermal conductivity $k_{\mathrm{h}} = 0.024$ W/m/°C, specific heat $c_{\mathrm{v}} = 1005$ J/kg/°C and thermal expansion coefficient $\beta = 0.00343$ °C^{-1} (McQuillan et al., 1984). For thermal flow, there are two relevant dimensionless quantities. One is the Prandtl number defined as

$$\mathrm{Pr} = \frac{\nu}{\alpha} \tag{39}$$

which describes the ratio of momentum diffusivity $\nu = \mu/\rho$ to thermal diffusivity $\alpha = k_{\mathrm{h}}/\rho c$. The properties of dry air adopted here gives a Prandtl number equal to 0.71, which implies that the heat diffuses faster than momentum, leading to a more rapid temperature variation within fluid flow. Another important dimensionless quantity is the Rayleigh number given by

$$\mathrm{Ra} = \frac{g\beta(\Theta_0 - \Theta_1)l^3}{\nu\alpha} \tag{40}$$

where g is the gravity; $\Theta_0 - \Theta_1$ represents the temperature difference across the cavity and l is a characteristic length of the fluid domain. The Rayleigh number quantifies the tendency of a fluid to undergo convective motion due to thermal gradients. A larger Rayleigh number indicates more significant convection driven by buoyancy forces. In a zero-gravity environment, the fluid is free from external forces, resulting in a Rayleigh number of zero. Consequently, the combined conduction-convection process simplifies to pure conduction under this circumstance. In this sub-section, g is set to be zero in the numerical model to simulate pure heat conduction in fluid.

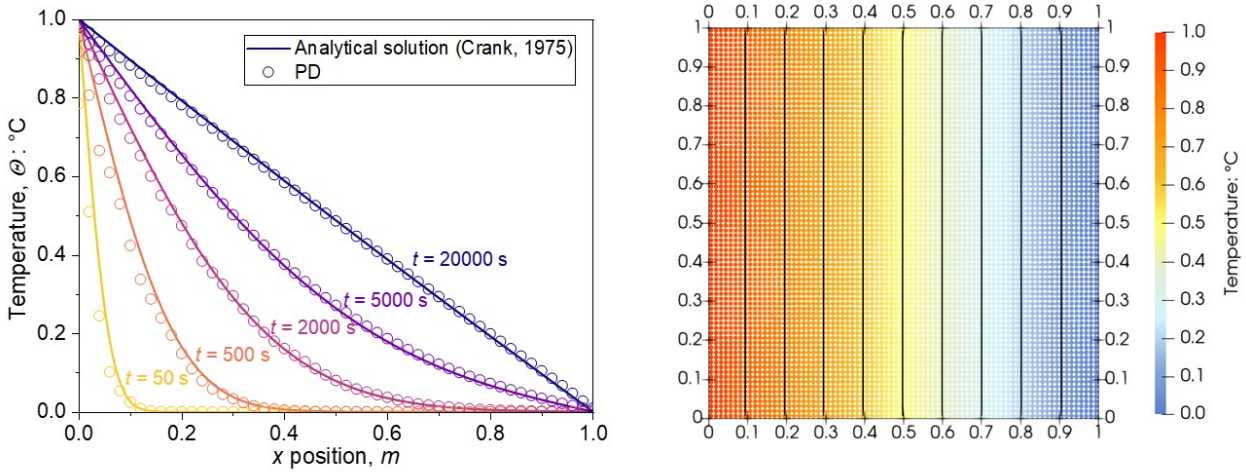

Fig. 6. (a) Comparison between PD results and analytical solution (Crank, 1975); and (b) temperature contour of simulation results after reaching steady state.

The transient heat distribution in a rectangular plate with such boundary conditions are analytically given by Crank (1975)

$$\Theta = \Theta_0 + (\Theta_1 - \Theta_0)\frac{x}{l} + \frac{2}{\pi}\sum_{n=1}^{\infty}\frac{\Theta_1 \cos n\pi - \Theta_0}{n}\sin\frac{n\pi x}{l}\, e^{-\frac{k_h n^2\pi^2 t}{\rho c\ \ l^2}} \tag{41}$$

By setting $\Theta_0 = 1$ °C and $\Theta_1 = 0$ °C, the analytical results along with the PD results at the central horizontal line, i.e., from point (0.0,0.5) to point (1.0,0.5), are shown in Fig. 6(a). The proposed coupled thermo-hydrodynamic PD method consistently matches well with the analytical

solution until reaching the steady state. Fig. 6(b) plots the temperature and position at each discretized material point, along with the temperature contour. It can be observed that all the material points nearly remain at their initial positions since there is no external force, and the thermal expansion is inapparent. The temperatures of material points with the same x position are the same as expected, resulting in a uniformly distributed vertical temperature contour. This example benchmarks the capability of the coupled thermo-hydrodynamic PD model in modeling the heat conduction process.

5.2 Natural convection in a closure

In this section, the same problem in Section 5.1 is re-considered by adding gravity force which is the driving force of natural convection phenomenon. De Vahl Davis (1983) indicates that the thermal flow becomes turbulent when Ra reach around 10^6. Therefore, three different Ra values, 10^3, 10^4, and 10^5, are simulated to investigate different patterns of convection. All the other setups are the same as adopted in Section 5.1.

Fig. 7 depicts temperature field for three different cases after reaching the steady state. Different from the results in Fig. 6(b), the isotherms are all distorted due to the convection process. Owing to the temperature variation, the density at left and top sides of the cavity would be smaller than the density at right and bottom sides. Therefore, the density variation further induces a buoyancy force that drives a clockwise circulation within the square cavity. As the Rayleigh number increases, the isotherms become more distorted. This phenomenon indicates a higher speed flow is generated for higher Ra number as validated by Fig. 8, in which the velocity distribution in x and y directions at steady state are shown. For convection with lower Ra number, the thermal flow involves a larger part of the material points while the velocity remains low. As a contrast, with a higher Ra number, the velocity of the thermal flow increases significantly while only the material points near the boundaries participate in the flow. These flow patterns and convective characters are consistent with the literature (Danis et al., 2013; Gao & Oterkus, 2019b; Szewc et al., 2011). Note that there are oscillations in the velocity field. This is mainly due to the explicit scheme and weakly compressible assumption adopted. The divergence of velocity in Eq. (10) cannot be guaranteed to be exactly zero in current scheme. The error may be mitigated by an implicit scheme or explicit incompressible scheme.

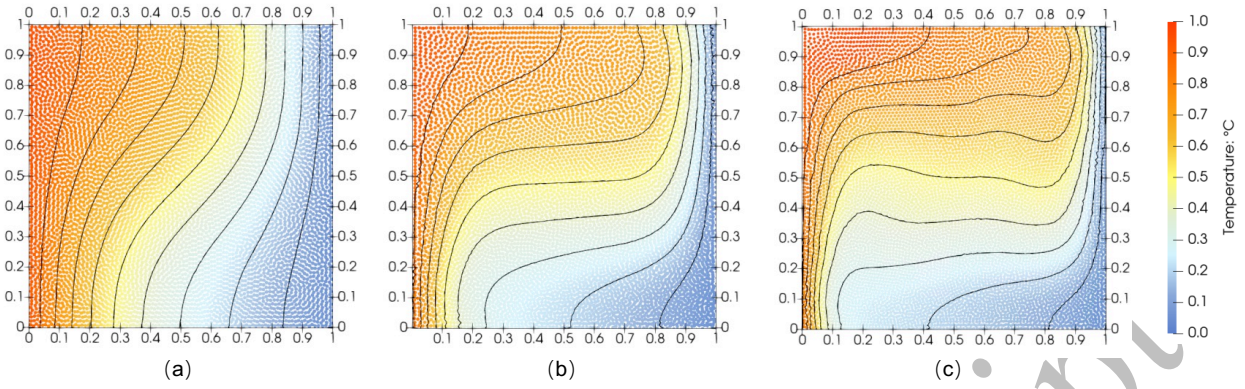

Fig. 7. Temperature distribution at each material point and temperature contour in the cavity for: (a) Ra = 10^3; (b) Ra = 10^4; and (c) Ra=10^5.

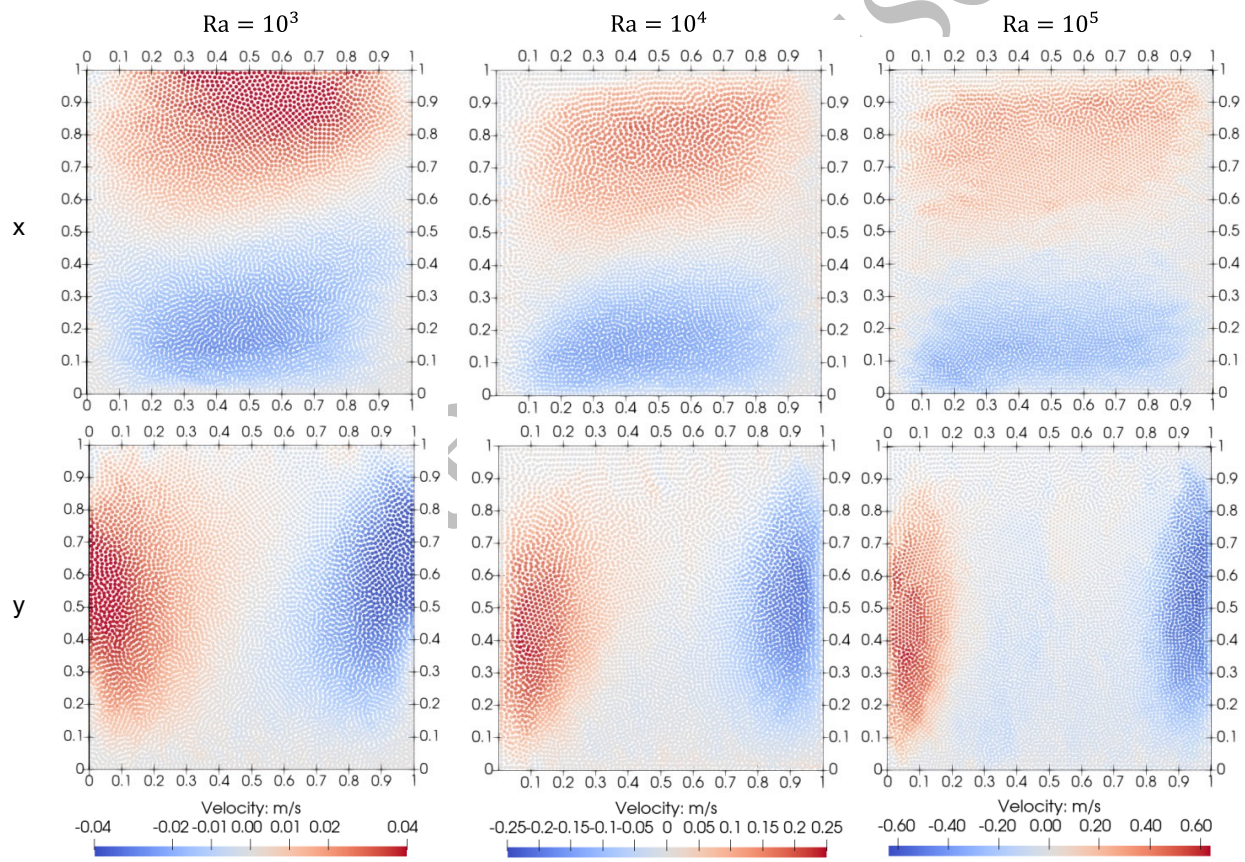

Fig. 8. Velocity distribution at each material point for: (a) Ra = 10^3; (b) Ra = 10^4; and (c) Ra=10^5.

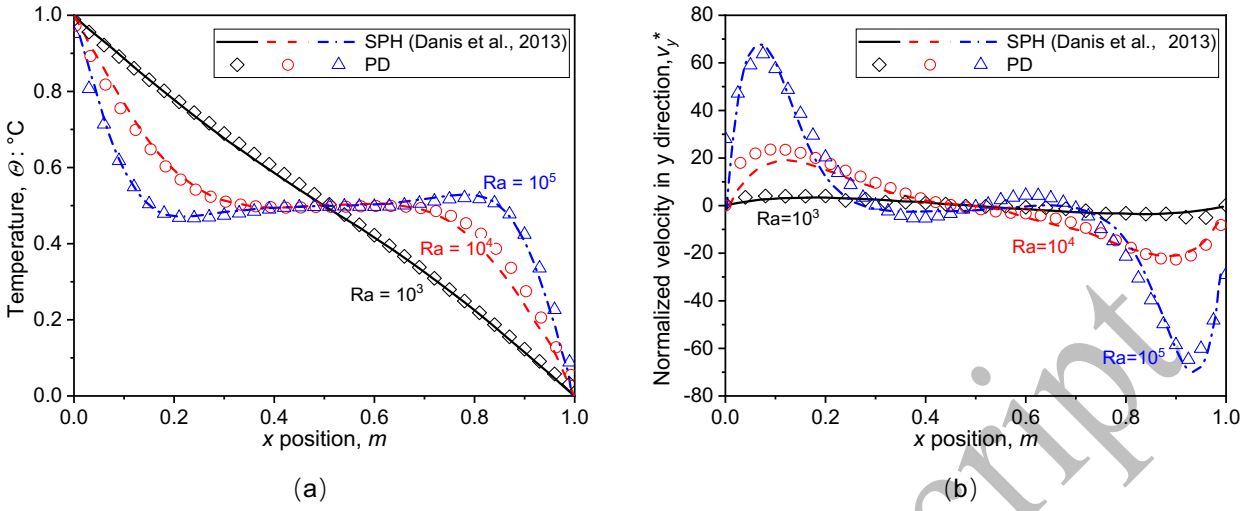

Fig. 9. Comparisons of (a) temperature and (b) normalized velocity in y direction along the central horizontal line for different Rayleigh numbers.

Quantitative comparisons between the proposed PD method and the SPH results along the central horizontal line of the square cavity, i.e., from point (0.0,0.5) to point (1.0,0.5), are shown in Fig. 9(a) and (b). When the Rayleigh number is relatively small, the convection is not significant, and the temperature approximately decreases linearly with the x position. As the Rayleigh number increases, the temperature distribution becomes a curve affected by the velocity of material points that boost or hinder the heat transfer. For all Rayleigh numbers, the temperature obtained from the proposed PD method match well with SPH results. To facilitate a comparison of velocity with Danis et al. (2013), we normalize the velocity in the same manner as:

$$v^* = \frac{v}{\alpha} = \frac{v\rho c}{k_{\mathrm{h}}} \tag{42}$$

As show in Fig. 9(b), the peak velocity increases significantly as Rayleigh number increases, which drives the convection process and makes the temperature contour more distorted. Again, both the trend and value of velocity are consistent with Danis et al. (2013).

In heat transfer analysis, the Nusselt number is another widely used dimensionless parameter to characterize the convective heat transfer between fluid and a solid surface. The local Nusselt number is defined as

$$\mathrm{Nu}(x) = \frac{\partial \Theta}{\partial x} \tag{43}$$

Note that although the boundaries are also modelled by fluid material points herein, it does not affect the validity of Nusselt number and its definition. The solid boundary can be applied by further developing coupled THM PD model, which serves as an interesting topic for future research. Fig. 10 plots the Nusselt number at the right wall, i.e., from point (1.0,0.0) to point (1.0,1.0), along with SPH results, where good agreements between the two methods are observed for all Rayleigh numbers.

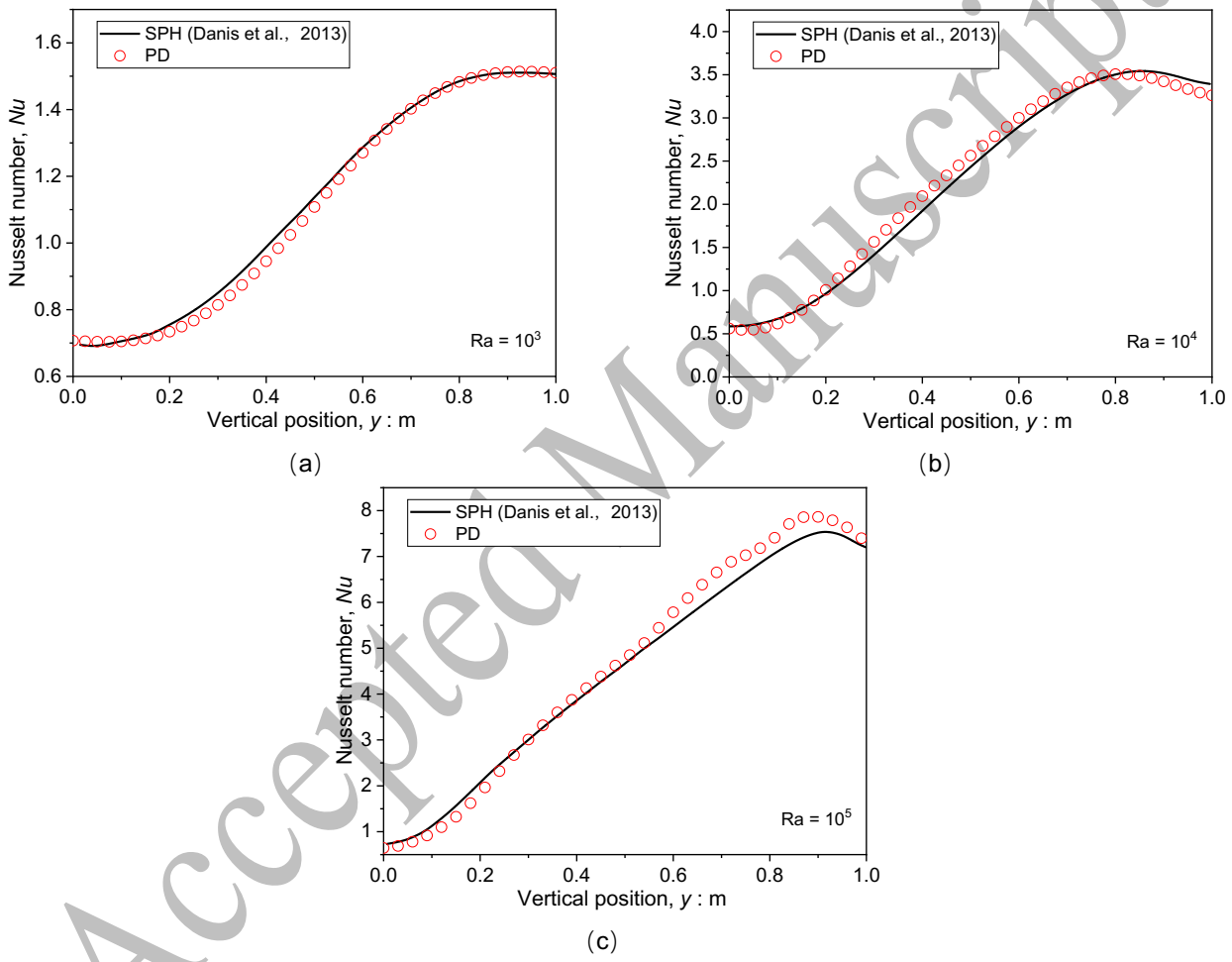

Fig. 10. Comparisons of Nusselt number at right wall for: (a) Ra = 10^3; (b) Ra = 10^4; and (c) Ra=10^5.

6 Numerical example and discussions

Another typical natural convection is Rayleigh-Bénard convection, which occurs in a planar horizontal layer of fluid heated from below as shown in Fig. 11(a). Different from the cases investigated in Sections 5.1 and 5.2, the gravity force in Rayleigh-Bénard convection is in line

with the initial temperature gradient. The Rayleigh-Bénard convection can develop a regular pattern of fluid flow known as Rayleigh-Bénard cell. The formation of such convection cell is still attributed to the density different due to temperature variation and hence buoyancy. The initial movement is the upwelling of less-dense fluid from the warmer bottom layer. The Rayleigh-Bénard convection holds significant importance in various fields. For instance, it is utilized to explain intricate patterns of frost damage in turfgrass (Ackerson et al., 2015). In the realm of biochemistry, the Rayleigh-Bénard convection cell is employed for polymerase chain reaction (PCR) processes (Krishnan et al., 2002; Yao et al., 2007), where a steady roll-type convective flow is required to duplicate DNA. In such cases, the temperature gradient between the bottom and top plates plays a crucial role in governing the convection. The Rayleigh number, which is associated with the temperature gradient, must be sufficiently large to initiate convection while avoiding excessive values that could cause turbulent flow. Additionally, without proper cell size design, the possibility of generating multi-roll flows emerges. Consequently, the utilization of numerical simulations offers significant benefits in exploring and understanding these phenomena in greater detail.

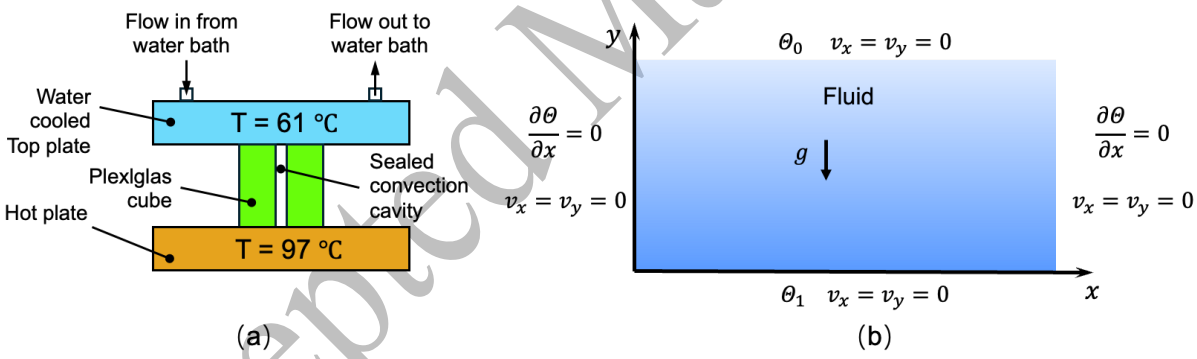

Fig. 11. Rayleigh-Bénard convection cell: (a) schematic (side view) of an experimental device by Krishnan et al. (2002); and (b) sketch map and boundaries conditions of PD model.

6.1 PD simulation of Rayleigh-Bénard convection

6.1.1 Roll pattern

Herein, the proposed thermo-hydrodynamic PD model is used to model a Rayleigh-Bénard convection cell as shown in Fig. 11(b). The right and left walls of the cell are assumed to be adiabatic. The bottom wall is maintained at a higher temperature denoted as Θ_1, while the top wall is subjected to a lower one Θ_0. All four surfaces are fixed by setting the velocity in both x and y

directions to zero. The properties of the fluid in this case are summarized as follows: density $\rho = 975$ kg/m^3, viscosity $\mu = 0.000377$ Pa·s, thermal conductivity $k_h = 6.71$ W/m/°C, specific heat $c_v = 4.176$ J/kg/°C, and thermal expansion coefficient $\beta = 0.0005$ °C^{-1}. Note that the properties are selected based on water given in Yao et al. (2007) with the specific heat capacity minimized and the thermal conductivity magnified to obtain a more regular convective pattern. Different temperature difference between top and bottom walls and different cell sizes are used to produce different convective patterns and showcase the capability of the proposed PD method.

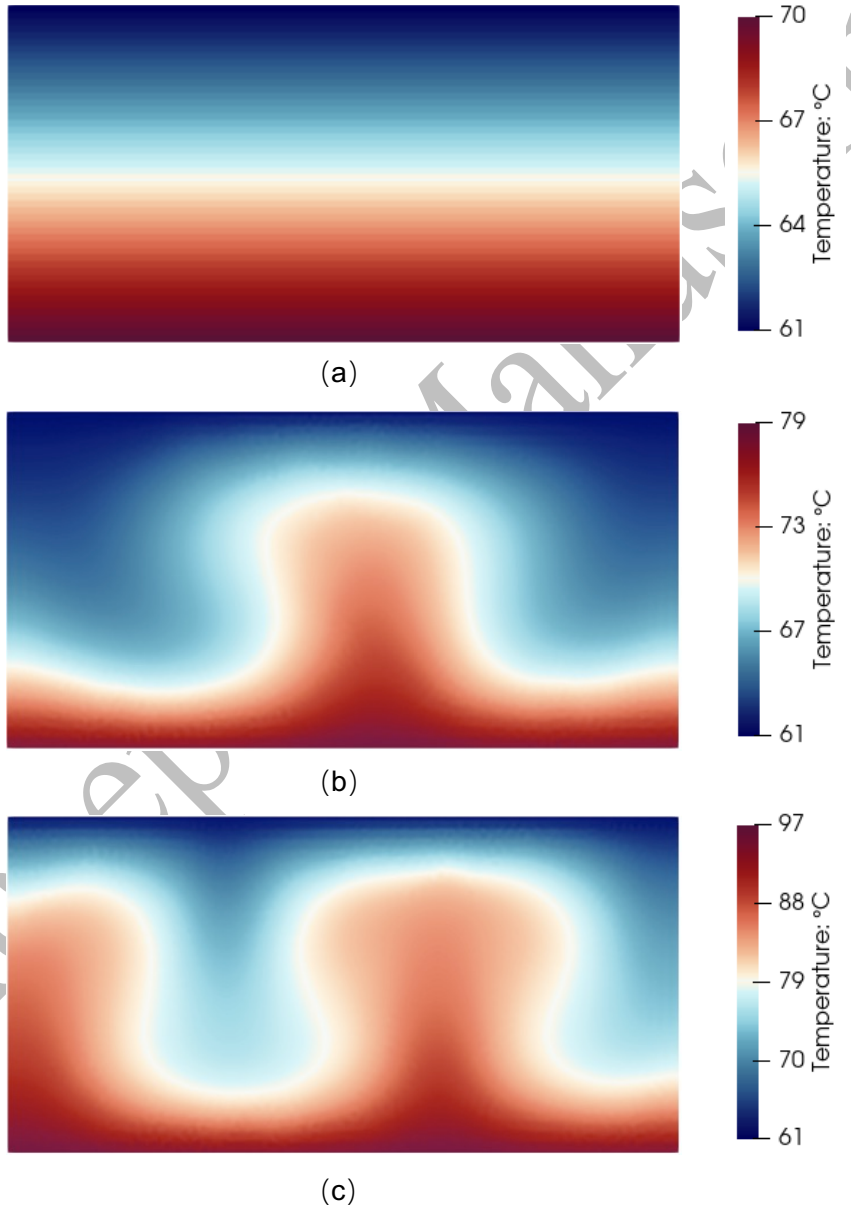

Fig. 12. Temperature distribution at steady state in the cell for (a) $\Theta_0 = 61$ °C and $\Theta_1 = 70$ °C; (b) $\Theta_0 = 61$ °C and $\Theta_1 = 79$ °C; and (c) $\Theta_0 = 61$ °C and $\Theta_1 = 97$ °C.

We first investigate a horizontally layered fluid cell with a width-to-height ratio of 2 as shown in Fig. 12. If the variation of temperature between the top and bottom plates is minor, the Rayleigh number is below the critical threshold that would trigger the convection, and the heat transport remains purely conductive. The temperature distributes linearly along the height after reaching the steady state. As the Rayleigh number increases, the pure conductive phase is broken up due to the tendency of upward movement of the heated fluid with lower density. These thermals have a mushroom-like appearance as indicated by the temperature fronts shown in Figs. 12(b) and 12(c), which is consistent with the phenomenological model proposed by Howard (1966) and experiment conducted by Sparrow et al. (1970). Finally, steady double-roll and triple-roll flows are formed for lower and higher Rayleigh number cases, respectively. The velocity of each material point is represented in Fig. 13 using arrows. The colormap represents the density of corresponding material point and saturates at higher and lower densities (a linear blue-white-red scale representing values from low to high).

It can be observed that the thermal flow initiates from hot fluid with lower densities towards cold region with higher densities, which once again demonstrates the crucial role of buoyancy force in natural convection. Such eruption moves colder fluid close to the bottom wall to replace the hot fluid. As the cold fluid is heated through conduction from the wall, it eventually triggers another such eruption. This cyclical process repeats, giving rise to a roll-type flow pattern. The rotation of the flows alternates horizontally between clockwise and counterclockwise. The rolls in Fig. 13(a) are approximately circular in shape while those in Fig. 13(b) appear to be more oval-shaped. This observation suggests a correlation between the Rayleigh number and the shape of the rolls. A higher Rayleigh number corresponds to thermals with increased velocity, which results in a more significant upward movement of the temperature front. Consequently, the rolls tend to take on an elliptical shape, with a longer axis in the vertical direction. In other words, the higher the Rayleigh number, the more elongated or stretched the rolls become vertically. This also explains why three rolls are formed in Figs. 12(b) and 13(b). The eruption is initiated around the position at $x = 0.65$ to form the second and third rolls (from right to left) in Fig. 13(b). Since both the second and third rolls are elliptical and there are still enough room in the right side of the cell for the formation of another complete roll, the first roll later is triggered and formed by the downward movement at the right edge of the second roll. Further increase in the temperature applied on bottom wall results in a turbulent and chaotic flow, which will be explored in detail in later cases. Note that although the geometry of model and boundary conditions are completely symmetric, the steady flow pattern is not. This phenomenon holds true in experiments where spatially random-distributed upward thermals are observed (Sparrow et al., 1970; Tritton, 1988) and the Rayleigh-

562 Bernard convection is known as one of the typical spontaneous symmetry breaking processes. In
563 terms of numerical modeling, the symmetry of the material points is disrupted after displacements
564 induced by heat conduction and convection. On the other hand, small numerical perturbations may
565 be amplified owing to the non-local nature of the PD theory. To some extent, this simulation results
566 reflect the reality lying in the symmetry breaking process of Rayleigh-Bernard convection.

567

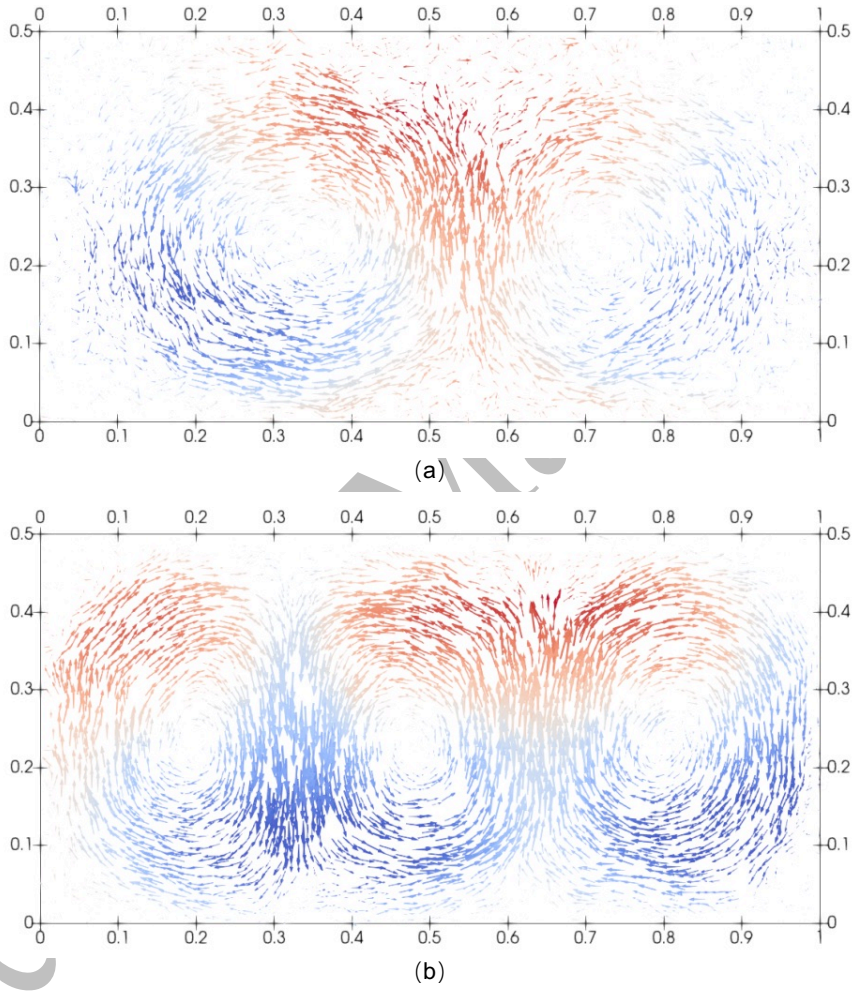

568

569 **Fig. 13**. Velocity field at steady state in the cell for (a) $\Theta_0 = 61$ °C and $\Theta_1 = 79$ °C; (b) $\Theta_0 = 61$ °C and
570 $\Theta_1 = 97$ °C. The direction and magnitude of arrows align with the direction and magnitude of velocity,
571 respectively. The arrows are colored by density.

572

573 With the temperature of the top and bottom plates kept at 61 °C and 97 °C, respectively,
574 different cell dimensions are adopted to investigate the effects of cell size. The results for width-
575 to-height ratio of 1, 2 and 3 are shown in Figs. 14(a)-(c). For these three cases, the Rayleigh

numbers are the same and the only differences lies in the width of the cell. The flow at steady state recovers from multi-roll type to single-roll type as the width-to-height ratio decreases, which is in line with the experimental finding by Krishnan et al. (2002). Such presence of a single steady roll, as depicted in Fig. 14(a), is advantageous for processes such as PCR. When the width-to-height ratio of the cell is set to 0.5 by doubling the height, the Rayleigh number of the cell in Fig. 14(d) is eight times of that in the other cases in Fig. 14(a)-(c). Consequently, the flow pattern becomes irregular and cannot reach a stable state. The temperature distribution and streamlines at different times are shown in Fig. 15. The initial thermal flux wanders upward instead of moving vertically as seen in Figs. 14(a)-(c). Subsequently, another new thermal flux emerges and disrupts the original flow. As a result, small-scale disorganized motions coexist alongside the larger-scale circulatory flow, leading to continuous interactions between them. The cell finally forms one single distorted thermal as shown in Figs. 15(d)-(f). Although the general shape of the thermal remains similar, this thermal flux still moves continuously with a certain period akin to the swaying of seaweed in water. This behavior is more clearly elucidated in Fig. 15(k)-(l), where the evolution of streamlines highlights the ongoing movement within the system.

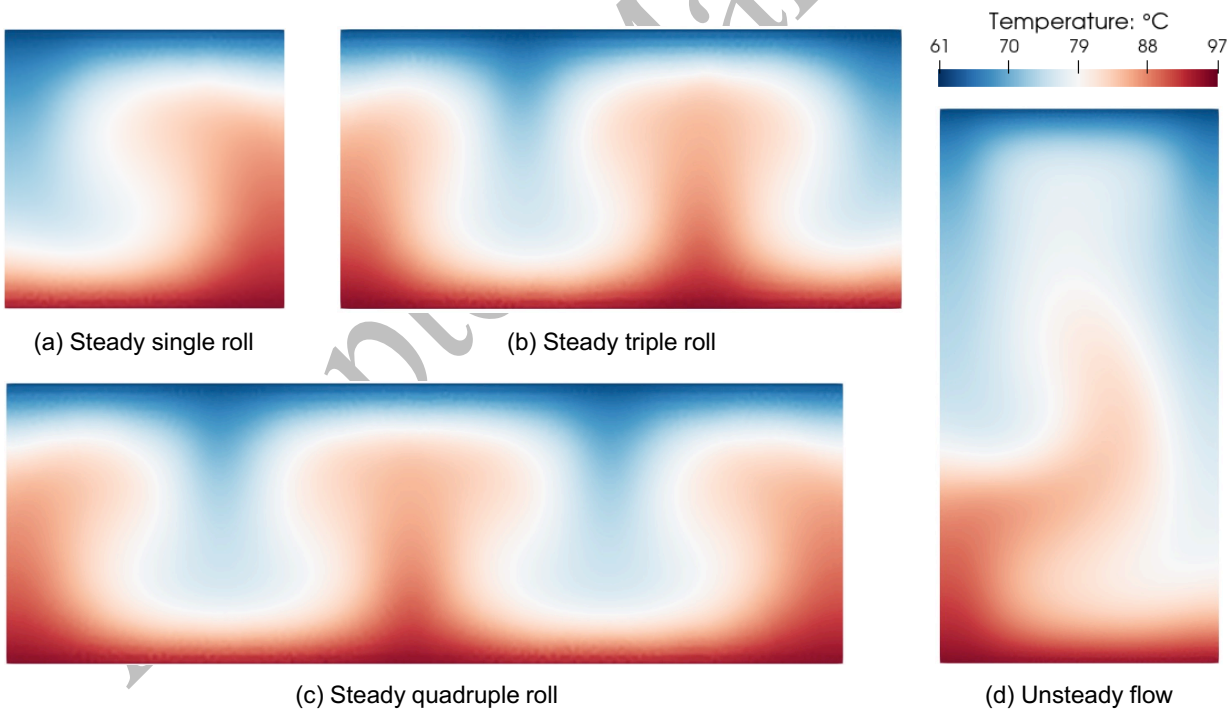

Fig. 14. Temperature distribution and roll type within the cell for different width-to-heigh ratios: (a) 1; (b) 2; (c) 3 and (d) 0.5.

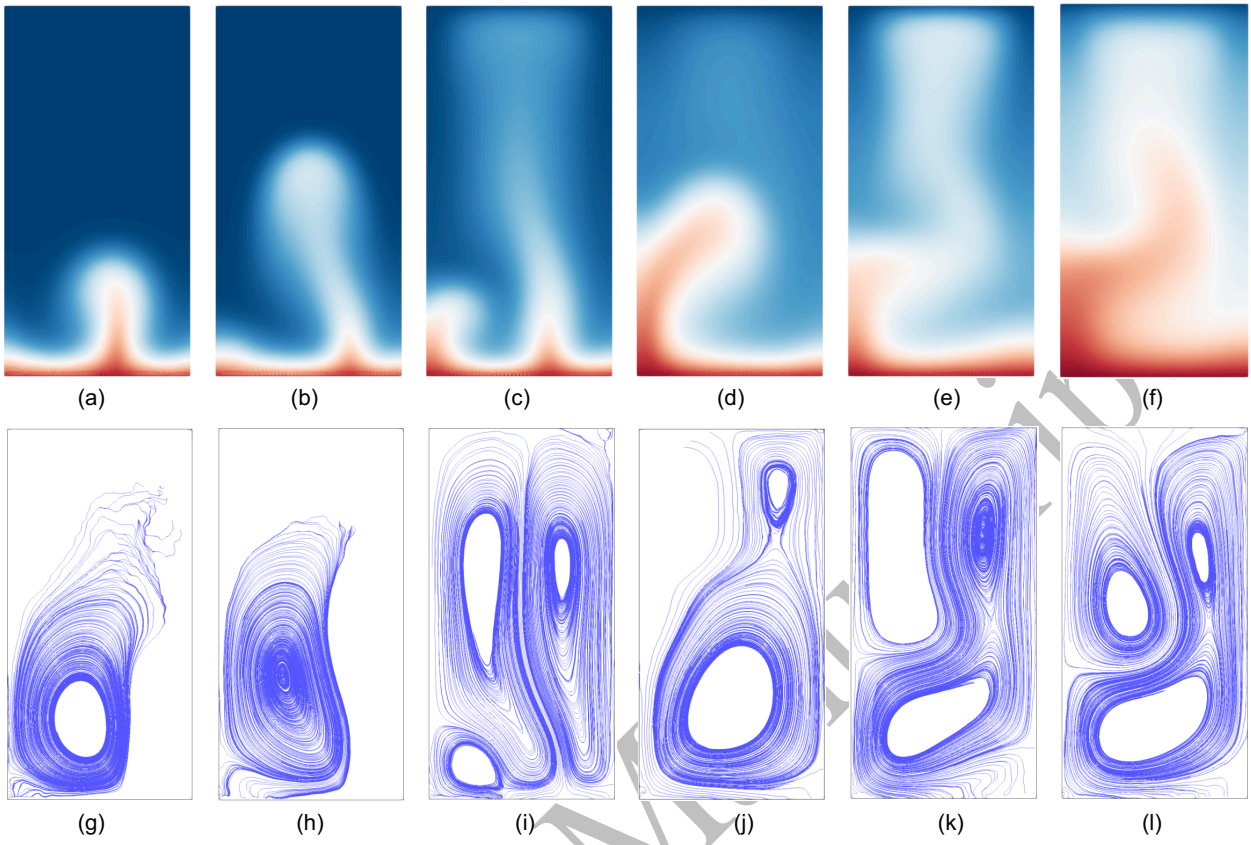

Fig. 15. Temperature distribution at (a) 5 s; (b) 6 s; (c) 10s; (d) 16 s; (e) 20 s and (f) 50 s; and streamlines at (g) 5 s; (h) 6 s; (i) 10s; (j) 16 s; (k) 20 s and (l) 50 s for the case in Fig. 14(d). Refer to the legend in Fig. 14.

6.1.2 Turbulent thermal flow

To further validate the proposed PD computational method and demonstrate its capability in modeling turbulent thermal flows at high Rayleigh numbers, we numerically reproduce the Rayleigh-Bénard convection experiment conducted by Sparrow et al. (1970), as shown in Fig. 16. In the experiment, a heating plate of 9 cm in width was positioned 8 cm above the bottom of a tank. The dimensions of the tank are 58 cm in width and 40 cm in height. The tank was filled with water at an initial temperature equal to $\Theta_0 = 23.6$ °C. The plate was gradually heated to $\Theta_1 = 43.1$ °C and maintained at this temperature. The experimental setup results in a Rayleigh number up to 10^{10}. For the simulation, we used the actual specific heat capacity and thermal conductivity of water. The experimental observations indicated that the fluid motion and temperature variation on the two sides and below the heating plate were minimal shortly after the heating commenced. Therefore, to optimize computational efficiency, we focus on the region above the heating plate

by selecting a simulation domain of 12 cm in width and 30 cm in height, as illustrated in Fig. 16. The material point size is set to 0.6 mm, resulting in a total of 104,236 material points.

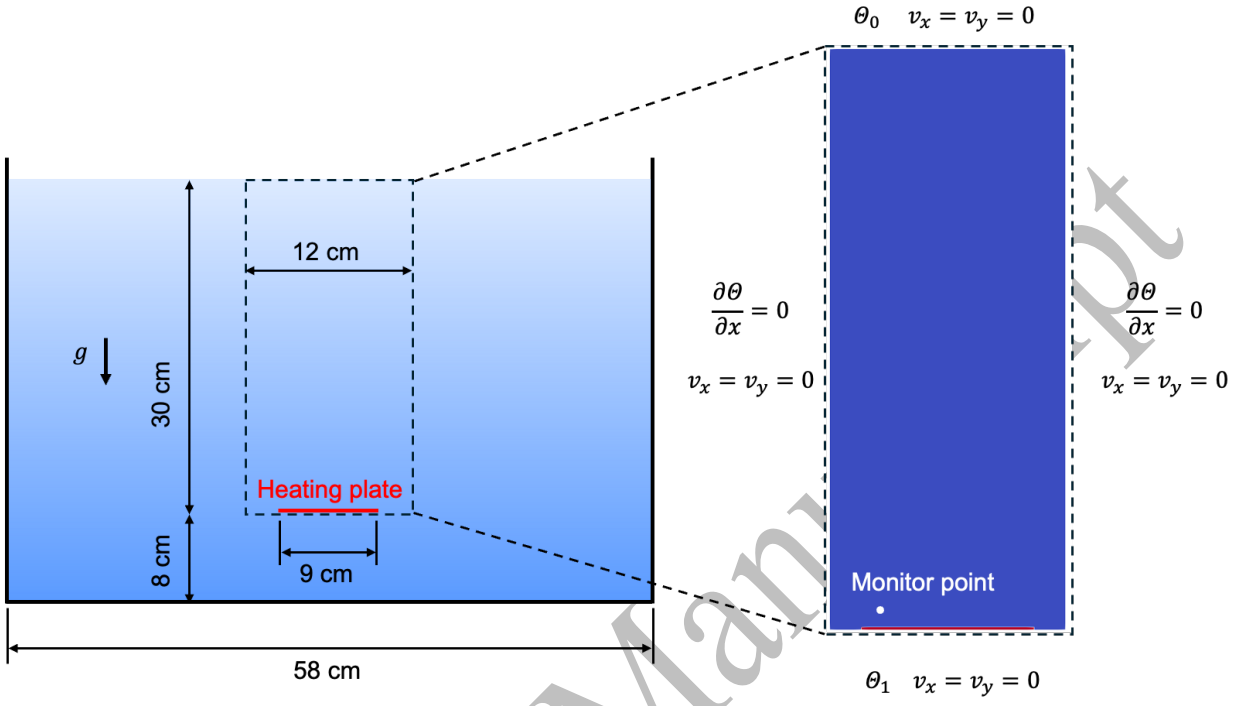

Fig. 16. Schematic of experimental setup in Sparrow et al. (1970) and numerical model.

In Fig. 17, it can be seen that the cellular pattern shown in previous cases is completely gone. These thermals lose their regularity as they ascend. The heights of different thermals are also different. Nevertheless, all thermals manifest as rising columns of fluid, spaced more or less evenly along the expanse of the heated surface. As a thermal ascends through the relatively calm surroundings fluid, its leading edge becomes blunted and folded back, resulting in a nearly semi-spherical cap and bestowing a mushroom-like appearance upon the thermal. Once these characteristics are established, the locations where the thermals originate appear to be fixed. In other words, subsequent generations of thermals emerge consistently from the same predetermined sites. These characteristics are consistent with the experimental results shown in Fig. 17(c), where the generations of thermals are in evidence. Fig. 18 illustrates the temperature evolution at the monitor point indicated in Fig. 16. This monitor point is located 0.8 cm above the heating plate, positioned above an active thermal. In the experiment, a thermocouple junction was placed at this location to record temperature changes. The experimental results show that the temperature oscillates with a nearly constant amplitude and a specific frequency, indicating that thermals are generated at almost consistent locations. The periodicity of the oscillations obtained from our

numerical results generally aligns well with the experimental recordings. However, the numerical results exhibit slight deviations from strict periodicity and constant amplitude. These discrepancies may be attributed to the smaller simulation domain that was adopted. Another possible reason is that the mesh resolution may be insufficient to fully resolve the interactions between nearby thermals, potentially leading to potential interference between them.

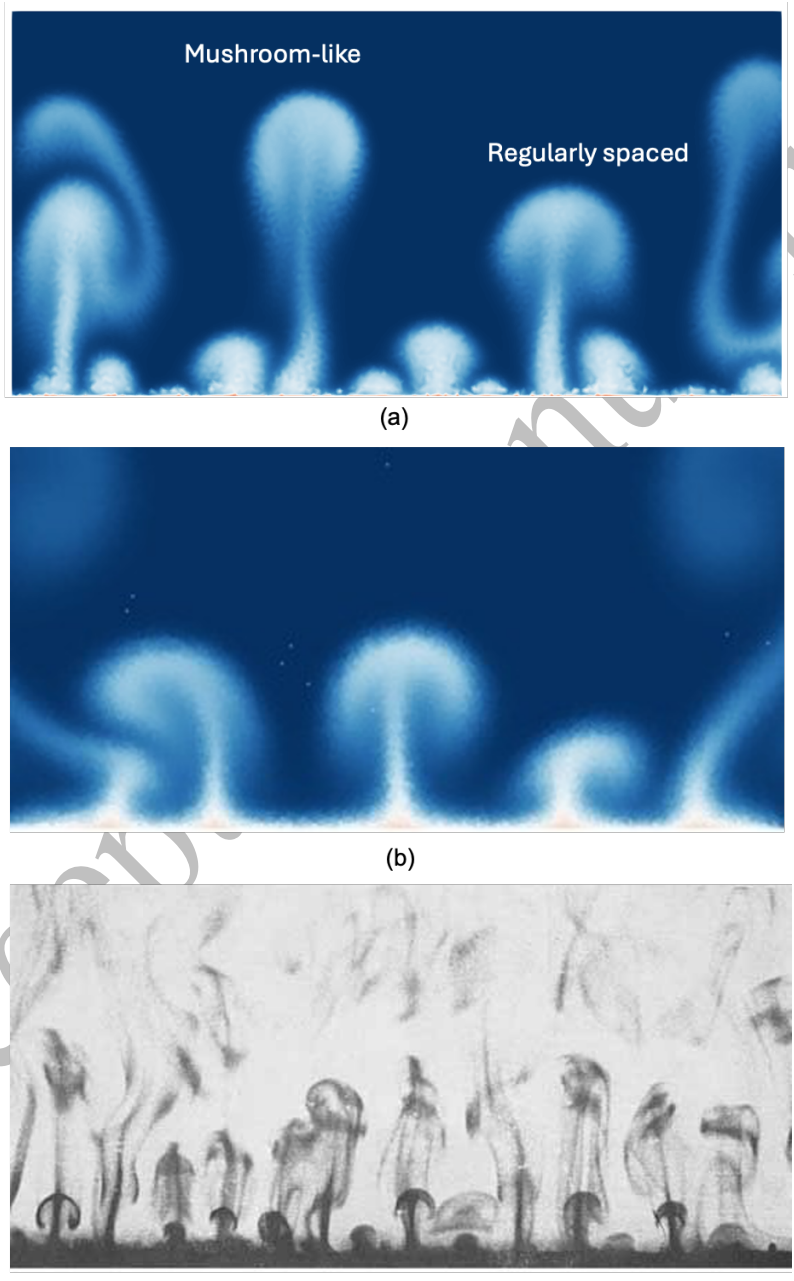

Fig. 17. Thermals rising from a heating plate: (a) numerical results obtained from PD; (b) numerical results obtained from SPH; and (b) experimental results (Sparrow et al., 1970).

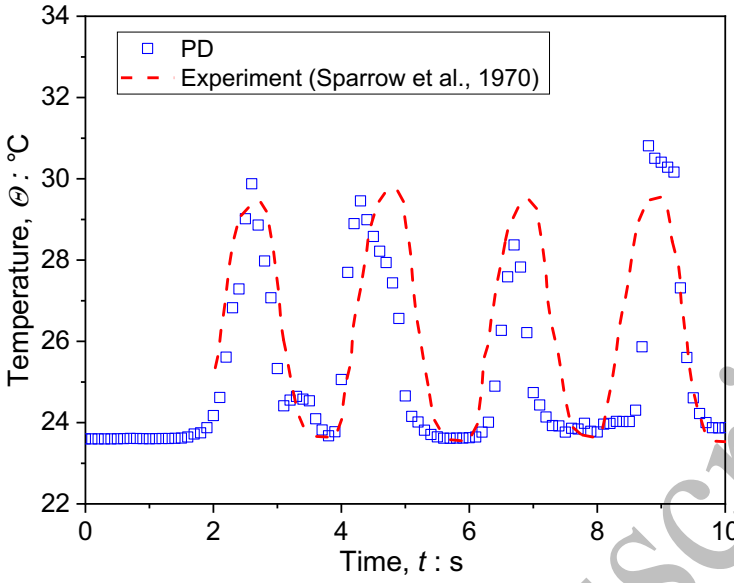

Fig. 18. Temperature evolution at a specific point above the heating plate.

6.2 Discussion: performance and limitations

A key concern regarding the proposed PD method is its computational efficiency. Common fluids, such as water, exhibit low thermal conductivity and high specific heat capacity, which often necessitates significant time to reach steady-state flow or display typical flow patterns. Achieving this with an explicit time integration scheme can lead to substantial computational costs.

To assess the computational efficiency of the proposed PD method, we compare its performance with that of SPH for the turbulent Rayleigh-Bénard convection case. PD and SPH share several similarities that make them suitable for comparison; both are particle-based methods that rely on interactions between particles. While PD is primarily known for its application in solid mechanics, SPH is widely used for fluid modeling. For this comparison, we reproduce the coupled thermo-hydrodynamic SPH method reported by Reece et al. (2024). To ensure a fair comparison, both PD and SPH employ explicit time integration schemes, identical model setups, and the same time step sizes. Additionally, the interaction range for both methods, defined as the horizon in PD and the smoothing length in SPH, is set to three times the particle size. For the turbulent Rayleigh-Bénard convection case, parallel computing is employed using 12 cores of an Intel® Xeon® Gold 6248 @ 3 GHz processor. The numerical result generated by SPH is presented in Fig. 17(b). Both PD and SPH qualitatively capture the mushroom-shaped thermals. However, based on our current results, SPH appears to produce fewer thermals compared to PD.

Table 1. Computational time comparison between PD and SPH

Case	No of particles	Steps	PD	SPH
Turbulent Rayleigh-Bénard convection	104,236	500,000	169,037 s	55,687 s
Natural convection with Ra = 10^3	7,396	5,000,000	134,518 s	162,974 s
Natural convection with Ra = 10^4	7,396	5,000,000	183,647 s	161,683 s
Natural convection with Ra = 10^5	7,396	5,000,000	192,777 s	163,988 s

Natural convection cases are also simulated using SPH, with computations performed on a single core of the same CPU. The computational times for the different cases, using both PD and SPH, are summarized in Table 1. From this table, it can be observed that the computational efficiency of PD is comparable to that of SPH for coupled thermo-hydrodynamic problems when using a single thread. However, PD exhibits lower efficiency than SPH when parallel computing is utilized. This difference can be attributed to several factors: the governing equations in PD, particularly for state-based formulations, are more complex than those in SPH, leading to higher computational overhead. Furthermore, SPH has been extensively used and optimized over several decades, especially in fluid dynamics. As a relatively newer method, PD has not yet benefited from the same level of algorithmic optimization and parallelization efforts as SPH.

Nevertheless, it is important to acknowledge that the efficiency of particle-based method, whether PD or SPH, is generally lower than that of element-based method such as FEM and FVM when modelling internal flows. The primary advantages of particle-based methods lie in their ability to handle free-surface flows and fluid-solid interaction problems with evolving geometries. Unlike element-based methods, which use Eulerian meshes and cannot precisely identify the position of free surfaces within an element, particle-based methods naturally and accurately capture free surfaces. This capability makes them particularly well-suited for problems involving complex interfacial dynamics.

One potential solution to further improve efficiency of PD is to employ an implicit scheme (Bie et al., 2019), which would allow for much larger time step. Additionally, the semi-Lagrangian formulation necessitates neighbor searches at each step arises, which can consume more time than the actual model computations in CPU-based codes. In this context, GPU-accelerated computing (Wang & Yin, 2024; Wang et al., 2025) also emerges as a promising approach. While these

technical considerations are intriguing, they delve more into the computer science and coding aspects, warranting dedicated future research. The primary focus here is more on the fluid mechanics aspect and the development of the coupled thermo-hydrodynamic formulation within a unified PD framework.

It should be emphasized that the Rayleigh number in the Rayleigh-Bénard convection case reaches up to 10^{10}. According to Danis et al. (2013), thermal flows at such high Rayleigh numbers are inherently turbulent. While the proposed PD method demonstrates the ability to capture typical turbulent thermal flow patterns, its performance for cases with even higher Rayleigh numbers requires further investigation. Additionally, the current implementation does not incorporate a turbulence model. Although the results align reasonably with experimental observations, we anticipate that the accuracy of the simulations could be further enhanced by integrating a turbulence model into the PD framework. This integration would improve the capability of the method to resolve finer-scale turbulent structures and dynamics.

Another important aspect of the multi-horizon scheme that warrants exploration is its energy conservation property, which has not been explicitly addressed in the previous work (Yang et al., 2024a). An important assumption made in the present study is that kinetic energy and thermal energy are independent, conserving within their respective horizons. This assumption is fundamental, as fluid flow is primarily driven by internal buoyancy forces, and fluid displacement does not generate or dissipate heat. However, in two-way coupled thermo-hydrodynamic scenarios, such as the plastic flow of liquid metal, where heat generation or dissipation occurs due to fluid movement, ensuring energy conservation in the multi-horizon scheme poses an intriguing challenge that requires further investigation.

7 Conclusion and outlook

This paper presents a new thermo-hydrodynamic model developed within the stated-based Peridynamics (PD) framework. The semi-Lagrangian PD formulation is adopted for modeling large deformations of fluids. This formulation is extended to non-isothermal conditions by incorporating the energy equation, which governs the heat conduction within the fluids. The energy equation is transformed into a non-local form using non-local gradient and divergence operators to align with the PD formulation. Consequently, multi-physics analysis involving fluid flow with heat transfer can be effectively conducted within the framework. To mitigate the numerical oscillations in thermal fields and to reduce computational costs, a multi-horizon scheme is proposed for coupled thermo-hydrodynamic modeling, where a smaller horizon is adopted for the thermal field (i.e., temperature) and a larger horizon is used for the flow field (i.e., velocity,

acceleration). The proposed method is benchmarked against a pure conduction problem and a classical natural convection problem in closed cavity. Further applications demonstrate the capabilities of the coupled PD method in capturing complex thermal flow patterns, including steady roll-type flows and turbulent mushroom-like thermals, as evidenced by experiments. Quantitative comparisons between the numerical results and recorded experimental data on periodicity and frequency of turbulent thermal generation further validated the proposed method.

The proposed computational method paves the way for the future development of a unified framework for computational modeling of coupled THM processes for both solids and fluids, particularly in scenarios where evolving discontinuities in solids play a critical role. Such scenarios are commonly encountered in nature and engineering applications. For instance, magma-driven fracturing (Spence & Turcotte, 1985; Taddeucci et al., 2021) in crustal rocks serves as a typical example. Similarly, in geothermal energy exploitation, cool water is injected into hot dry rock to create a more interconnected fracture network. In these contexts, the intricate interplays between mechanical and thermal fracturing, heat conduction and convection in and across different phases, as well as fluid flow, must all be considered. The proposed PD method for fluid modeling can be seamlessly integrated with existing thermo-mechanical PD solid models, such as the one developed by Yang et al. (2024a), which is capable of modeling heat transfer in solids as well as fracture initiation and propagation. Since both fluid and solid components can be modeled within a single particle-based framework, there is no need to explicitly define the fluid-solid interface. This represents a significant advantage when addressing complex, evolving geometries in fluid-structure interaction problems. Furthermore, coupling PD fluid and solid models does not require specialized techniques. A straightforward fictitious point method (Yang et al., 2024b) can be employed to complete the horizons of interacting solid and fluid material points. This unified framework can be further extended to incorporate phase change processes between fluid and solid, enabling the modeling and interpretation of many intriguing phenomena in geoscience, such as igneous process and rainfall- or temperature-induced fracture initiation and propagation in glaciers.

Acknowledgments

The study was financially supported by the National Science Foundation of China (through project 11972030) and Research Grants Council of Hong Kong (through GRF project 16212724, CRF project C7082-22G, TRS projects T22-607/24N and T22-606/23-R). Fan Zhu acknowledges support from JSPS KAKENHI Grant Number 23K13403. Changyi Yang acknowledges financial support from the Hong Kong Ph.D. Fellowship Scheme funded by Research Grants Council of Hong Kong.

References

Ackerson, B. J., Beier, R. A., & Martin, D. L. (2015). Ground level air convection produces frost damage patterns in turfgrass. *International Journal of Biometeorology*, *59*(11), 1655–1665. https://doi.org/10.1007/s00484-015-0972-3

Angeli, D., Levoni, P., & Barozzi, G. S. (2008). Numerical predictions for stable buoyant regimes within a square cavity containing a heated horizontal cylinder. *International Journal of Heat and Mass Transfer*, *51*(3), 553–565. https://doi.org/10.1016/j.ijheatmasstransfer.2007.05.007

Aragón, F., Guzmán, J. E. V., Alvarado-Rodríguez, C. E., Sigalotti, L. D. G., Carvajal-Mariscal, I., Klapp, J., & Uribe-Ramírez, A. R. (2021). Smoothed Particle Hydrodynamics Modeling of Natural Convection Around a Heated Horizontal Cylinder: A Comparison With Experiments. *Journal of Heat Transfer*, *143*(042601). https://doi.org/10.1115/1.4049495

Bazazzadeh, S., Mossaiby, F., & Shojaei, A. (2020). An adaptive thermo-mechanical peridynamic model for fracture analysis in ceramics. *Engineering Fracture Mechanics*, *223*, 106708. https://doi.org/10.1016/j.engfracmech.2019.106708

Behzadinasab, M., & Foster, J. T. (2020). A semi-Lagrangian constitutive correspondence framework for peridynamics. *Journal of the Mechanics and Physics of Solids*, *137*, 103862. https://doi.org/10.1016/j.jmps.2019.103862

Bell, B. C., & Surana, K. S. (1995). *P*-Version least squares finite element formulation for two-dimensional incompressible Nnewtonian and non-Newtonian non-isothermal fluid flow. *Computers & Structures*, *54*(1), 83–96. https://doi.org/10.1016/0045-7949(94)E0280-F

Bergel, G. L., & Li, S. (2016). The total and updated lagrangian formulations of state-based peridynamics. *Computational Mechanics*, *58*(2), 351–370. https://doi.org/10.1007/s00466-016-1297-8

Bie, Y., Li, S., Hu, X., & Cui, X. (2019). An implicit dual-based approach to couple peridynamics with classical continuum mechanics. *International Journal for Numerical Methods in Engineering*, *120*(12), 1349–1379. https://doi.org/10.1002/nme.6182

Bie, Y., Ren, H., Bui, T. Q., Madenci, E., Rabczuk, T., & Wei, Y. (2024). Dual-horizon peridynamics modeling of coupled chemo-mechanical-damage for interface oxidation-induced cracking in thermal barrier coatings. *Computer Methods in Applied Mechanics and Engineering*, *430*, 117225. https://doi.org/10.1016/j.cma.2024.117225

Bie, Y., Ren, H., Rabczuk, T., Quoc Bui, T., & Wei, Y. (2024). The fully coupled thermo-mechanical dual-horizon peridynamic correspondence damage model for homogeneous and heterogeneous materials. *Computer Methods in Applied Mechanics and Engineering*, *420*, 116730. https://doi.org/10.1016/j.cma.2023.116730

Chen, D., Huang, W., & Huang, D. (2024). A study of overtopping breach process with soil–water erosion using improved smoothed particle hydrodynamics. *Acta Geotechnica*, *19*(2), 939–951. https://doi.org/10.1007/s11440-023-01979-1

Chen, D., Huang, W., & Liang, C. (2024). A three-dimensional smoothed particle hydrodynamics analysis of multiple retrogressive landslides in sensitive soil. *Computers and Geotechnics*, *170*, 106284. https://doi.org/10.1016/j.compgeo.2024.106284

Chen, W., Gu, X., Zhang, Q., & Xia, X. (2021). A refined thermo-mechanical fully coupled peridynamics with application to concrete cracking. *Engineering Fracture Mechanics*, *242*, 107463. https://doi.org/10.1016/j.engfracmech.2020.107463

Cleary, P. W., & Monaghan, J. J. (1999). Conduction Modelling Using Smoothed Particle Hydrodynamics. *Journal of Computational Physics*, *148*(1), 227–264. https://doi.org/10.1006/jcph.1998.6118

Cormack, D. E., Leal, L. G., & Seinfeld, J. H. (1974). Natural convection in a shallow cavity with differentially heated end walls. Part 2. Numerical solutions. *Journal of Fluid Mechanics*, *65*(2), 231–246. https://doi.org/10.1017/S0022112074001364

Crank, J. (1975). *The mathematics of diffusion* (2d ed). Clarendon Press.

Danis, M. E., Orhan, M., & Ecder, A. (2013). ISPH modelling of transient natural convection. *International Journal of Computational Fluid Dynamics*, *27*(1), 15–31. https://doi.org/10.1080/10618562.2012.753146

De Vahl Davis, G. (1983). Natural convection of air in a square cavity: A bench mark numerical solution. *International Journal for Numerical Methods in Fluids*, *3*(3), 249–264. https://doi.org/10.1002/fld.1650030305

Diyaroglu, C. (2016). *Peridynamics and its applications in marine structures*.

Drummond, J. E., & Korpela, S. A. (1987). Natural convection in a shallow cavity. *Journal of Fluid Mechanics*, *182*(1), 543. https://doi.org/10.1017/S0022112087002453

Du, J., Chen, H., Li, Q., Huang, Y., & Hong, Y. (2024). Turbulent flow-thermal-thermodynamic characteristics of a solar air heater with spiral fins. *International Journal of Heat and Mass Transfer*, *226*, 125434. https://doi.org/10.1016/j.ijheatmasstransfer.2024.125434

Gao, Y., & Oterkus, S. (2019a). Fully coupled thermomechanical analysis of laminated composites by using ordinary state based peridynamic theory. *Composite Structures*, *207*, 397–424. https://doi.org/10.1016/j.compstruct.2018.09.034

Gao, Y., & Oterkus, S. (2019b). Non-local modeling for fluid flow coupled with heat transfer by using peridynamic differential operator. *Engineering Analysis with Boundary Elements*, *105*, 104–121. https://doi.org/10.1016/j.enganabound.2019.04.007

Garoosi, F., & Shakibaeinia, A. (2020). Numerical simulation of entropy generation due to natural convection heat transfer using Kernel Derivative-Free (KDF) Incompressible Smoothed Particle Hydrodynamics (ISPH) model. *International Journal of Heat and Mass Transfer*, *150*, 119377. https://doi.org/10.1016/j.ijheatmasstransfer.2020.119377

Gartling, D. K. (1977). Convective heat transfer analysis by the finite element method. *Computer Methods in Applied Mechanics and Engineering*, *12*(3), 365–382. https://doi.org/10.1016/0045-7825(77)90024-X

Gui, N., Zhang, X., Huang, X., Yang, X., Tu, J., & Jiang, S. (2022). SPH simulation of natural convection in a modeled reactor core using a new combinatorial kernel. *Annals of Nuclear Energy*, *175*, 109249. https://doi.org/10.1016/j.anucene.2022.109249

Hao, D. H., Liu, Q.-Q., Hu, Y. L., Madenci, E., Guo, H., & Yu, Y. (2024). Coupled neutronic–thermal–mechanical analysis of a nuclear fuel pellet using peridynamics. *Engineering with Computers*. https://doi.org/10.1007/s00366-023-01930-8

Howard, L. N. (1966). Convection at high Rayleigh number. In H. Görtler (Ed.), *Applied Mechanics* (pp. 1109–1115). Springer. https://doi.org/10.1007/978-3-662-29364-5_147

Huang, J. M. (2024). Covering convection with a thermal blanket: Numerical simulation and stochastic modelling. *Journal of Fluid Mechanics*, *980*, A47. https://doi.org/10.1017/jfm.2023.1071

Kim, B. S., Lee, D. S., Ha, M. Y., & Yoon, H. S. (2008). A numerical study of natural convection in a square enclosure with a circular cylinder at different vertical locations. *International Journal of Heat and Mass Transfer*, *51*(7), 1888–1906. https://doi.org/10.1016/j.ijheatmasstransfer.2007.06.033

Krishnan, M., Ugaz, V. M., & Burns, M. A. (2002). PCR in a Rayleigh-Bénard Convection Cell. *Science*, *298*(5594), 793–793. https://doi.org/10.1126/science.298.5594.793

Macek, R. W., & Silling, S. A. (2007). Peridynamics via finite element analysis. *Finite Elements in Analysis and Design*, *43*(15), 1169–1178. https://doi.org/10.1016/j.finel.2007.08.012

Madenci, E., Barut, A., & Dorduncu, M. (2019). *Peridynamic Differential Operator for Numerical Analysis*. Springer International Publishing. https://doi.org/10.1007/978-3-030-02647-9

Madenci, E., & Oterkus, E. (2014). *Peridynamic Theory and Its Applications*. Springer New York. https://doi.org/10.1007/978-1-4614-8465-3

Mallinson, G. D., & Davis, G. D. V. (1977). Three-dimensional natural convection in a box: A numerical study. *Journal of Fluid Mechanics*, *83*(1), 1–31. https://doi.org/10.1017/S0022112077001013

McQuillan, F. J., Culham, J. R., & Yovanovich, M. M. (1984). Properties of dry air at one atmosphere. *Microelectronics Heat Transfer Lab*. https://sv.20file.org/up1/1101_0.pdf

Monaghan, J. J. (1994). Simulating Free Surface Flows with SPH. *Journal of Computational Physics*, *110*(2), 399–406. https://doi.org/10.1006/jcph.1994.1034

Paolucci, S. (1990). Direct numerical simulation of two-dimensional turbulent natural convection in an enclosed cavity. *Journal of Fluid Mechanics*, *215*(1), 229. https://doi.org/10.1017/S0022112090002634

Prabhakar, V., & Reddy, J. N. (2006). Spectral/*hp* penalty least-squares finite element formulation for the steady incompressible Navier–Stokes equations. *Journal of Computational Physics*, *215*(1), 274–297. https://doi.org/10.1016/j.jcp.2005.10.033

Reddy, J. N., & Gartling, D. K. (2010). *The Finite Element Method in Heat Transfer and Fluid Dynamics* (0 ed.). CRC Press. https://doi.org/10.1201/9781439882573

Reece, G., Rogers, B. D., Fourtakas, G., & Lind, S. (2024). Buoyancy-driven circulation and multi-component mixing using SPH with a new adiabatic boundary condition. *International Journal of Heat and Mass Transfer*, *233*, 125904. https://doi.org/10.1016/j.ijheatmasstransfer.2024.125904

Shi, K., Zhu, F., & Zhao, J. (2022). Multi-scale analysis of shear behaviour of crushable granular sand under general stress conditions. *Géotechnique*, 1–18. https://doi.org/10.1680/jgeot.21.00412

Silling, S. A. (2000). Reformulation of elasticity theory for discontinuities and long-range forces. *Journal of the Mechanics and Physics of Solids*, *48*(1), 175–209. https://doi.org/10.1016/S0022-5096(99)00029-0

Silling, S. A., & Askari, E. (2005). A meshfree method based on the peridynamic model of solid mechanics. *Computers & Structures*, *83*(17), 1526–1535. https://doi.org/10.1016/j.compstruc.2004.11.026

Silling, S. A., Epton, M., Weckner, O., Xu, J., & Askari, E. (2007). Peridynamic States and Constitutive Modeling. *Journal of Elasticity*, *88*(2), 151–184. https://doi.org/10.1007/s10659-007-9125-1

Silling, S. A., Parks, M. L., Kamm, J. R., Weckner, O., & Rassaian, M. (2017). Modeling shockwaves and impact phenomena with Eulerian peridynamics. *International Journal of Impact Engineering*, *107*, 47–57. https://doi.org/10.1016/j.ijimpeng.2017.04.022

Sparrow, E. M., Husar, R. B., & Goldstein, R. J. (1970). Observations and other characteristics of thermals. *Journal of Fluid Mechanics*, *41*(4), 793–800. https://doi.org/10.1017/S0022112070000927

Spence, D. A., & Turcotte, D. L. (1985). Magma-driven propagation of cracks. *Journal of Geophysical Research: Solid Earth*, *90*(B1), 575–580. https://doi.org/10.1029/JB090iB01p00575

Szewc, K., Pozorski, J., & Tanière, A. (2011). Modeling of natural convection with Smoothed Particle Hydrodynamics: Non-Boussinesq formulation. *International Journal of Heat and Mass Transfer*, *54*(23), 4807–4816. https://doi.org/10.1016/j.ijheatmasstransfer.2011.06.034

Taddeucci, J., Cimarelli, C., Alatorre-Ibargüengoitia, M. A., Delgado-Granados, H., Andronico, D., Del Bello, E., Scarlato, P., & Di Stefano, F. (2021). Fracturing and healing of basaltic magmas during explosive volcanic eruptions. *Nature Geoscience*, *14*(4), Article 4. https://doi.org/10.1038/s41561-021-00708-1

Tang, L. Q., & Tsang, T. T. H. (1997). Temporal, spatial and thermal features of 3-D Rayleigh-Bénard convection by a least-squares finite element method. *Computer Methods in Applied Mechanics and Engineering*, *140*(3), 201–219. https://doi.org/10.1016/S0045-7825(96)01053-5

Trias, F. X., Soria, M., Oliva, A., & Pérez-Segarra, C. D. (2007). Direct numerical simulations of two- and three-dimensional turbulent natural convection flows in a differentially heated cavity of aspect ratio 4. *Journal of Fluid Mechanics*, *586*, 259–293. https://doi.org/10.1017/S0022112007006908

Tritton, D. J. (1988). *Physical fluid dynamics* (2nd ed). Clarendon Press ; Oxford University Press.

Tu, Q., & Li, S. (2017). An updated Lagrangian particle hydrodynamics (ULPH) for Newtonian fluids. *Journal of Computational Physics*, *348*, 493–513. https://doi.org/10.1016/j.jcp.2017.07.031

van Heerden, A. S. J., Judt, D. M., Jafari, S., Lawson, C. P., Nikolaidis, T., & Bosak, D. (2022). Aircraft thermal management: Practices, technology, system architectures, future challenges, and opportunities. *Progress in Aerospace Sciences*, *128*, 100767. https://doi.org/10.1016/j.paerosci.2021.100767

Vazic, B., Diyaroglu, C., Oterkus, E., & Oterkus, S. (2020). Family Member Search Algorithms for Peridynamic Analysis. *Journal of Peridynamics and Nonlocal Modeling*, *2*(1), 59–84. https://doi.org/10.1007/s42102-019-00027-5

Wang, X., & Yin, Z.-Y. (2024). Interpretable physics-encoded finite element network to handle concentration features and multi-material heterogeneity in hyperelasticity. *Computer Methods in Applied Mechanics and Engineering*, *431*, 117268. https://doi.org/10.1016/j.cma.2024.117268

Wang, X., Yin, Z.-Y., Wu, W., & Zhu, H.-H. (2025). Differentiable finite element method with Galerkin discretization for fast and accurate inverse analysis of multidimensional heterogeneous engineering structures. *Computer Methods in Applied Mechanics and Engineering*, *437*, 117755. https://doi.org/10.1016/j.cma.2025.117755

Wang, Y., & Qin, G. (2018). An improved time-splitting method for simulating natural convection heat transfer in a square cavity by Legendre spectral element approximation. *Computers & Fluids*, *174*, 122–134. https://doi.org/10.1016/j.compfluid.2018.07.013

Wang, Y., Zhou, X., & Kou, M. (2018). A coupled thermo-mechanical bond-based peridynamics for simulating thermal cracking in rocks. *International Journal of Fracture*, *211*(1), 13–42. https://doi.org/10.1007/s10704-018-0273-z

Xue, Y., Liu, S., Chai, J., Liu, J., Ranjith, P. G., Cai, C., Gao, F., & Bai, X. (2023). Effect of water-cooling shock on fracture initiation and morphology of high-temperature granite: Application of hydraulic fracturing to enhanced geothermal systems. *Applied Energy*, *337*, 120858. https://doi.org/10.1016/j.apenergy.2023.120858

Yan, J., Li, S., Kan, X., Zhang, A.-M., & Liu, L. (2021). Updated Lagrangian particle hydrodynamics (ULPH) modeling of solid object water entry problems. *Computational Mechanics*, *67*(6), 1685–1703. https://doi.org/10.1007/s00466-021-02014-4

Yan, J., Li, S., Zhang, A.-M., Kan, X., & Sun, P.-N. (2019). Updated Lagrangian Particle Hydrodynamics (ULPH) modeling and simulation of multiphase flows. *Journal of Computational Physics*, *393*, 406–437. https://doi.org/10.1016/j.jcp.2019.05.017

Yang, C., Zhu, F., & Zhao, J. (2024a). A multi-horizon fully coupled thermo-mechanical peridynamics. *Journal of the Mechanics and Physics of Solids*, *191*, 105758. https://doi.org/10.1016/j.jmps.2024.105758

Yang, C., Zhu, F., & Zhao, J. (2024b). Coupled total- and semi-Lagrangian peridynamics for modelling fluid-driven fracturing in solids. *Computer Methods in Applied Mechanics and Engineering*, *419*, 116580. https://doi.org/10.1016/j.cma.2023.116580

Yang, X., & Kong, S.-C. (2019). Numerical study of natural convection in a horizontal concentric annulus using smoothed particle hydrodynamics. *Engineering Analysis with Boundary Elements*, *102*, 11–20. https://doi.org/10.1016/j.enganabound.2019.02.007

Yao, D.-J., Chen, J.-R., & Ju, W.-T. (2007). Micro-Rayleigh-Bénard convection polymerase chain reaction system. *Journal of Micro/Nanolithography, MEMS, and MOEMS*, *6*(4), 043007. https://doi.org/10.1117/1.2805452

Yao, X., Chen, D., Wu, L., & Huang, D. (2023). A multi-resolution DFPM-PD model for efficient solution of FSI problems with structural deformation and failure. *Engineering Analysis with Boundary Elements*, *157*, 424–440. https://doi.org/10.1016/j.enganabound.2023.09.023

Yao, X., & Huang, D. (2022). Coupled PD-SPH modeling for fluid-structure interaction problems with large deformation and fracturing. *Computers & Structures*, *270*, 106847. https://doi.org/10.1016/j.compstruc.2022.106847

Yu, J., Zhao, J., Liang, W., & Zhao, S. (2024a). A semi-implicit material point method for coupled thermo-hydro-mechanical simulation of saturated porous media in large deformation. *Computer Methods in Applied Mechanics and Engineering*, *418*, 116462. https://doi.org/10.1016/j.cma.2023.116462

963 Yu, J., Zhao, J., Liang, W., & Zhao, S. (2024b). Multiscale modeling of coupled thermo-hydro-
964 mechanical behavior in ice-bonded granular media subject to freeze-thaw cycles.
965 *Computers and Geotechnics*, *171*, 106349.
966 https://doi.org/10.1016/j.compgeo.2024.106349
967 Yu, J., Zhao, J., Zhao, S., & Liang, W. (2024c). Thermo-hydro-mechanical coupled material point
968 method for modeling freezing and thawing of porous media. *International Journal for*
969 *Numerical and Analytical Methods in Geomechanics*, *n/a*(n/a).
970 https://doi.org/10.1002/nag.3794
971 Yu, T., & Zhao, J. (2022). Quantitative simulation of selective laser melting of metals enabled by
972 new high-fidelity multiphase, multiphysics computational tool. *Computer Methods in*
973 *Applied Mechanics and Engineering*, *399*, 115422.
974 https://doi.org/10.1016/j.cma.2022.115422
975 Zhang, H., & Zhang, X. (2022). Peridynamic analysis of materials interface fracture with thermal
976 effect. *Theoretical and Applied Fracture Mechanics*, *120*, 103420.
977 https://doi.org/10.1016/j.tafmec.2022.103420
978 Zhang, W., & Yang, X. (2022). SPH modeling of natural convection in horizontal annuli. *Acta*
979 *Mechanica Sinica*, *39*(4), 322093. https://doi.org/10.1007/s10409-022-22093-x
980 Zhu, F., & Zhao, J. (2019a). A peridynamic investigation on crushing of sand particles.
981 *Géotechnique*, *69*(6), 526–540. https://doi.org/10.1680/jgeot.17.P.274
982 Zhu, F., & Zhao, J. (2019b). Modeling continuous grain crushing in granular media: A hybrid
983 peridynamics and physics engine approach. *Computer Methods in Applied Mechanics and*
984 *Engineering*, *348*, 334–355. https://doi.org/10.1016/j.cma.2019.01.017
985 Zhu, F., & Zhao, J. (2021). Peridynamic modelling of blasting induced rock fractures. *Journal of*
986 *the Mechanics and Physics of Solids*, *153*, 104469.
987 https://doi.org/10.1016/j.jmps.2021.104469
988